

Feature Lottery? A Bifurcation Theory of Concept Emergence

Fuming Yang*

MIT

Abstract

Neural networks acquire structured representations at specific moments during training, yet identifying these transitions typically relies on retrospective, label-dependent metrics. We introduce a bifurcation theory of representation dynamics to detect these moments in real time. By analyzing a passive GMM probe attached to the evolving encoder, we show that the onset of structure can be identified with a supercritical pitchfork bifurcation driven by the loss Hessian. The system exhibits a theoretically predictable zero-crossing (β_c) that, compared to the network’s current state (β), yields a dynamic ratio $\beta(t)/\beta_c(t)$. This ratio acts as a universal, label-free phase coordinate for representation dynamics computable entirely from hidden states.

We empirically validate four distinct transition regimes predicted by this coordinate across diverse settings: SAEs on language models (Pythia), SSL (CIFAR), and grokking (modular arithmetic). Crucially, under finite dissipation, the macroscopic symmetry-breaking can lag the initial zero-crossing by orders of magnitude: providing a rigorous dynamical account of the delayed escape observed in grokking. At the microscopic level, the theory predicts that the bifurcation creates a shared unstable subspace, forcing a collective symmetry breaking. We term this the *feature lottery* in SAE training: a feature’s terminal interpretability becomes predictable remarkably early. By only 5% of training, early atom purity robustly predicts final convergence purity, with top-decile early atoms achieving over $12\times$ the baseline purity at the end of training.

Beyond explaining concept emergence, β/β_c provides a highly practical tool. It functions as an early-warning indicator for training health: detecting the onset of usable structure, the crystallization of feature identity, and the onset of representational collapse epochs before downstream metrics react.

Interactive demo: <https://fumingyang-felix.github.io/feature-lottery-demo/>

1 Introduction

Modern networks do not merely fit labels or reconstruct inputs; during training, their internal states reorganize into discrete, reusable directions that behave like concepts. Yet we typically notice this reorganization only after the fact: by probing with labels, by inspecting downstream accuracy, or by mechanistic analysis of a fully trained model. What is missing is a *label-free dynamical signal* of when such concept structure first becomes available, a quantity that (watched live during training) tells us whether and when a network has just acquired a usable internal representation, and ideally *which* parts of the representation are about to become meaningful.

*Correspondence to: fumingy@mit.edu

Our angle. We provide such a signal, derived from a single Hessian analysis. Attach a passive K -prototype isotropic Gaussian-mixture (GMM) head with shared learned precision β to the output $z = \text{enc}(x)$ of a given encoder representation, and analyze the Hessian of its negative log-likelihood at the *symmetric collapsed state* $\mu_1 = \dots = \mu_K = \bar{z}$. The analysis (Section 3) yields a critical precision

$$\beta_c = \frac{1}{\lambda_{\max}(\text{Cov}(z))} \quad (1)$$

at which the lowest eigenvalue of the loss Hessian crosses zero; above β_c the prototypes pitchfork along the principal eigenvector of $\text{Cov}(z)$. We adopt this Hessian-pitchfork event as our *operational* definition of concept emergence: the moment at which the encoder’s representation first admits a class-aligned K -prototype decomposition. The label-free indicator is $\beta(t)/\beta_c(t)$, computable from the encoder’s hidden state and the GMM probe alone. When the encoder is itself learning, $\beta_c(t)$ becomes endogenous and we prove $\beta(t)$ and $\beta_c(t)$ must cross at some finite training time (Proposition 1). A subtlety, made precise in Remark 1, is that the crossing event marks when the symmetric state becomes *unstable*, not when the broken-symmetry state becomes *macroscopically observable*. The lag between the two is controlled by the encoder’s dissipation, and can range from essentially zero (in well-trained SSL) to thousands of steps (in grokking).

The sharpest prediction is per-atom. At the crossing event, the unstable subspace at $\beta = \beta_c$ is shared by all $K - 1$ anti-symmetric modes (App. A.2). The bifurcation is therefore a *collective* event with a *per-atom signature*: each atom must select a specific direction from a common unstable manifold, its choice driven by initialization noise and the cubic terms of the pitchfork normal form. This per-atom prediction is empirically sharp. In SAE training on frozen Pythia-160M layer 6, per-atom POS purity is at noise floor before the bifurcation and acquires predictive content at onset; ranking atoms by their step-1,000 POS purity (5% of training) already recovers a top decile whose convergence purity is $12\times$ the uniform-random baseline (Section 5). We refer to this as the SAE *feature lottery*, the bifurcation theory’s sharpest and most unexpected empirical consequence; it is the SAE-level analogue of the lottery-ticket framing of Frankle and Carbin [2019], with the drawing event identified explicitly as the first phase transition during training.

Contributions.

- Theory: an endogenous critical point with post-critical metastability.** A Hessian-pitchfork prediction of when a given encoder representation first admits a K -prototype decomposition, obtained from a passive GMM probe on the encoder output, with an existence proof for the endogenous critical point (Proposition 1; the crossing $\beta = \beta_c$ happens at a finite time *conditional on* the encoder eventually spreading the latent enough for the GMM to resolve clusters) and a separate prediction of post-critical metastability under finite dissipation (Remark 1). Both are new relative to the static soft- K -means criticality of Rose et al. [1990]: Rose gives the critical temperature on a frozen dataset; we give the dynamic crossing theorem when $\beta_c(t)$ co-evolves with the encoder, and identify a post-critical metastable regime that the static analysis cannot exhibit.
- The theory’s sharpest empirical consequence: an SAE feature lottery at 5% of training.** At the crossing event the unstable subspace is shared by all $K - 1$ anti-symmetric modes, so atoms must select directions from a common manifold during the bifurcation. We verify this in SAE training on frozen language-model activations (Sec. 5): per-atom POS purity is at noise floor pre-onset ($\rho_{\text{id}} \approx 0.03$), and by step 1,000 (5% of training), identity-matched $\rho_{\text{id}} = +0.41 \pm 0.04$ (3 seeds, all $p < 10^{-80}$). The top decile of atoms ranked at 5% achieves convergence POS purity 0.82 ± 0.03 , $12.3 \pm 0.4\times$ the uniform-random baseline of 0.067. The effect replicates across soft-L1 and architectural top- K SAEs, and across $K \in \{256, \dots, 8192\}$ with $\rho_{\text{id}} \in [0.26, 0.41]$. This is an atom-level, post-onset analogue of the lottery-ticket framing of Frankle and Carbin [2019].

3. **Empirical universality of the bifurcation arc.** The predicted trajectory in $(\log(\beta/\beta_c), \log \text{NC1})$ is governed by three binary kinematic axes: initial sub/supercriticality, the post-onset race between $\beta(t)$ and $\beta_c(t)$, and the dissipation rate (Sec. 4.3, App. I). The axes predict which kinematic regimes are accessible to which feature-learning methods. We verify the four regimes that arise in standard pipelines; full V (SAE on frozen Pythia layer 6), fold-back (DINO/SimCLR on CIFAR-10/100, with magnitude controlled by data complexity), delayed escape (grokking on modular arithmetic, with WD-monotonic escape time $\tau_{\text{esc}} \propto \text{WD}^{-1.23}$ across six WD levels, and 0/3 escape at WD=0), and no arc (rotation-prediction control).
4. **K-sweep: lottery is K -stable, POS-purity Pareto is K -monotonic but K -confounded.** At fixed 3% top- K sparsity, the lottery ρ_{id} is stable across $K \in \{256, \dots, 8192\}$ (range $[+0.26, +0.41]$). Per-atom POS purity decreases monotonically with K from 0.725 to 0.370 (Tab. 4), while reconstruction MSE moves the other way ($0.11 \rightarrow 0.015$). Because POS has only 15 classes, this purity-vs- K trend is partly structural: small- K atoms each correspond to coarser token-cluster partitions that more easily align with the 15-way POS partition. We therefore do *not* recommend small K on the basis of POS purity alone; a K -unbiased interpretability metric (e.g. causal mediation or LLM-as-judge) is required to make a substantive recommendation (Sec. 5.4).
5. **A label-free training diagnostic.** β/β_c identifies the encoder’s current act from hidden states alone, well before downstream metrics respond. In grokking, the indicator at step 100 already places the trajectory in Act 2: $\sim 8,400$ steps before `test_acc` moves. In DINO from-scratch with collapse modes (Sec. 6.1), β/β_c leads cluster accuracy by 8 epochs in the gradual mode; in mid-training interventions (Sec. 6.2) it responds within a single batch while training loss remains within noise.

2 Related work

Concept emergence and mechanistic interpretability. A growing body of work in mechanistic interpretability studies how internal computations of trained models implement particular “concepts.” Nanda et al. [2023] show that the post-grok solution of modular addition is a Fourier multiplication algorithm distributed across the network’s embedding, attention, and MLP layers; sparse autoencoders on frozen language-model activations [Bricken et al., 2023, Gao et al., 2025, Templeton et al., 2024] extract interpretable directions in feature space. These works identify concepts *post-hoc* on a trained model: features are evaluated for interpretability after training converges, and the typical assumption is that training longer yields better features. Our framework is complementary along two axes. First, we provide a label-free *dynamical* signal of when such structure first becomes available during training (Sec. 4). Second, we show that in SAEs the bifurcation onset is a per-atom assignment event whose outcome predicts atom-level interpretability nineteen thousand training steps in advance (Sec. 5). This reframes SAE feature emergence as a structured lottery rather than a gradual refinement.

Neural collapse. The neural-collapse literature [Papayan et al., 2020] and the subsequent Unconstrained Features Model analyses [Mixon et al., 2022, Tirer and Bruna, 2022, Zhou et al., 2022, Sůkeník et al., 2024] characterize the static terminal-phase geometry of supervised classification. Wang and Palmer [2023] recover an analogous structure in supervised contrastive learning via an information-bottleneck argument. These analyses describe the endpoint, not the dynamics by which an encoder reaches it; our framework supplies the missing dynamics and predicts the timing of concept emergence without labels.

Deterministic annealing and rate-distortion clustering. Rose et al. [1990] obtained the critical temperature $T_c = 2\lambda_{\max}(\Sigma)$ for soft K -means by externally annealing T . In our convention $\beta = 2/T$, this is the

external- β limit of our analysis. The novelty here is that β is endogenous and $\beta_c(t)$ moves with the encoder.

Self-supervised collapse. Jing et al. [2022], Hua et al. [2021] analyze dimensional collapse in contrastive and non-contrastive self-supervised methods. Caron et al. [2021] introduces DINO with centering and sharpening regularizers specifically to prevent collapse. Our diagnostic experiments (Sec. 6) take DINO collapse modes as a controlled testbed.

Grokking and emergence. Power et al. [2022] discovered that small transformers on modular arithmetic exhibit a long memorization plateau followed by a sudden generalization transition; Nanda et al. [2023] mechanistically identified the in-network DFT circuit responsible. The plateau-then-sudden-transition pattern is reminiscent of the saddle-to-saddle dynamics characterized in deep linear networks by Saxe et al. [2014], where learning proceeds through a sequence of loss-landscape saddles separated by long plateaus. Our framework gives this picture a concrete representation-geometric content: the plateau is the metastable post-critical regime ($\beta > \beta_c$ but ε still microscopic; Remark 1), and the dissipation strength sets the escape time. We revisit grokking in Sec. 4.2 as the cleanest empirical instance of post-critical metastability in our framework.

Phase transitions in deep learning. Wang and Ziyin [2022] analyzes posterior collapse in linear latent-variable models, and Ziyin and Ueda [2023] prove first- and second-order phase transitions in deep linear networks under a statistical-mechanics framing. Both connect collapse-type phenomena to phase transitions in regularized learning. We share this perspective and contribute a closed-form Hessian-based predictor of the transition point in unsupervised and self-supervised settings.

Lottery-ticket framing (weak analogy). Frankle and Carbin [2019] introduce the lottery-ticket hypothesis for supervised classifiers: there exist sparse subnetworks identifiable already at initialization that train to the same accuracy as the full network. Our finding for SAE atoms (Sec. 5) is a *weaker analogue* in feature space: early per-atom POS purity at the bifurcation onset is a useful ranking signal for converged per-atom POS purity (identity-matched Spearman $\rho = +0.41 \pm 0.04$ between step-1,000 and step-20,000). The analogy is weaker than Frankle and Carbin [2019] in two important senses: (1) identification happens at the post-onset bifurcation event rather than at initialization, and (2) achievement requires continued joint training, not isolated retraining of a sparse subnetwork. We use the lottery framing for its spirit (*what matters is decided early*), not as a structural isomorphism.

3 Theory

3.1 Setup

We attach a K -component isotropic GMM with shared precision β and component means $\mu_k \in \mathbb{R}^d$ to the encoder output $z = \text{enc}(x)$:

$$p(z | \theta) = \frac{1}{K} \sum_{k=1}^K \mathcal{N}(z | \mu_k, \beta^{-1}I), \quad \mathcal{L}_\mu(\mu, \beta) = -\mathbb{E}_z \left[\text{LSE}_k \left(-\frac{\beta}{2} \|z - \mu_k\|^2 \right) \right], \quad (2)$$

up to terms independent of μ . We denote the data covariance $\Sigma = \text{Cov}(z)$ with eigenvalues $\sigma_1^2 \geq \dots \geq \sigma_d^2$, the responsibilities $p(k | z) = \text{softmax}_k(-\frac{\beta}{2} \|z - \mu_k\|^2)$, and the symmetric collapsed state $\mathcal{S}_0 = \{\mu_k = \bar{z}\}$.

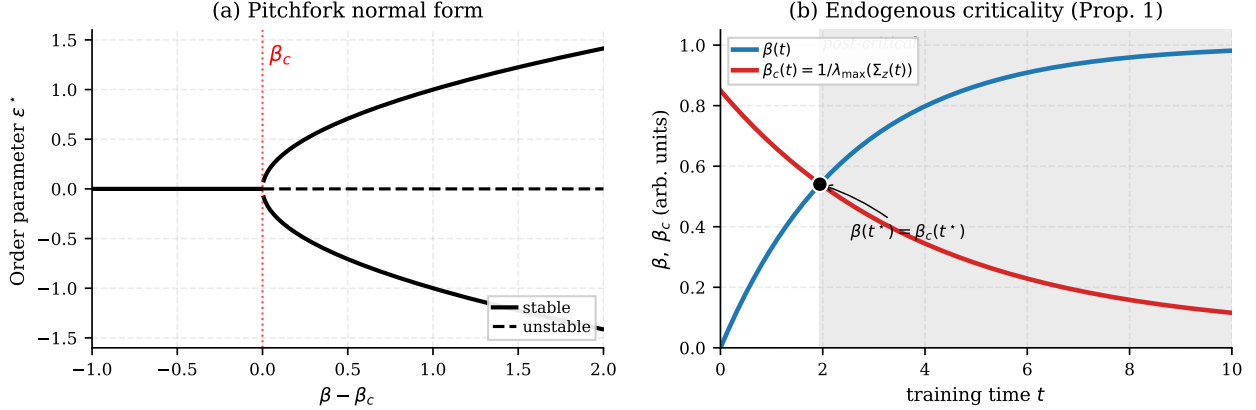


Figure 1: Theory. **(a)** The supercritical pitchfork at β_c : below β_c the symmetric collapsed state is stable; above β_c it becomes a saddle and two stable broken-symmetry branches emerge. **(b)** Endogenous criticality (Proposition 1): when the encoder is itself learning, $\beta_c(t)$ co-evolves with $\text{Cov}(z(t))$; under mild monotonicity assumptions $\beta(t)$ and $\beta_c(t)$ must cross at some finite time t^* .

3.2 Hessian at the symmetric state

At \mathcal{S}_0 we have $p(k|z) = 1/K$ and $\nabla_\mu \mathcal{L}_\mu = 0$. Differentiating once more and evaluating at \mathcal{S}_0 ,

$$\left. \frac{\partial^2 \mathcal{L}_\mu}{\partial \mu_k^a \partial \mu_l^b} \right|_{\mathcal{S}_0} = \frac{\beta}{K} \delta_{kl} \delta^{ab} - \frac{\beta^2}{K} \left(\delta_{kl} - \frac{1}{K} \right) \Sigma^{ab}. \quad (3)$$

Eigenvectors decompose into separable perturbations $\xi_l^b = w_l u^b$ with $w \in \mathbb{R}^K$ and $u \in \mathbb{R}^d$. Two channels arise: the symmetric channel (w constant) is always stable with eigenvalues β/K ; the anti-symmetric channel ($\sum_l w_l = 0$, $(K-1)$ -fold degenerate) has spatial eigenvalues

$$\lambda_i^\perp(\beta) = \frac{\beta}{K} (1 - \beta \sigma_i^2), \quad i = 1, \dots, d. \quad (4)$$

The lowest such eigenvalue is $\lambda_1^\perp(\beta) = (\beta/K)(1 - \beta \lambda_{\max}(\Sigma))$, and crosses zero exactly at the critical precision in equation 1. The unstable direction is the principal eigenvector of Σ in spatial space combined with any anti-symmetric w in component space. Projecting the dynamics onto this slow direction yields the supercritical pitchfork normal form

$$\dot{\varepsilon} = (\beta - \beta_c) \varepsilon - \alpha \varepsilon^3 + \text{noise}, \quad \alpha > 0, \quad (5)$$

shown in Fig. 1(a). A full derivation, including the parametrization correction relative to Rose et al. [1990] and the explicit eigendecomposition in component space (Theorem 1), is in Appendix A (§A.1).

3.3 Hierarchy and reverse traversal

The analysis recurses within each post-primary supercluster, giving a sequence of secondary critical precisions $\beta_c^{(2)} = 1/\lambda_{\max}(\Sigma_{\text{within}})$. The pitchfork equation 5 is also reversible: decreasing β continuously merges the broken-symmetry branches back into \mathcal{S}_0 . App. E confirms both on toy data (hierarchy to four decimals; forward overshoot $\beta^*/\beta_c \approx 1.3$, reverse tracking within $\leq 4\%$) and on CIFAR-scale encoders (App. F).

3.4 Endogenous criticality

Replace the fixed dataset $\{z_n\}$ with $\{z_n(t)\} = \{\text{enc}(x_n; \varphi(t))\}$, where the encoder parameters φ evolve under an upstream loss. The critical precision becomes time-dependent:

$$\beta_c(t) = \frac{1}{\lambda_{\max}(\text{Cov}(z(t)))}, \quad (6)$$

and the bifurcation occurs at the moment $\beta(t^*) = \beta_c(t^*)$.

Proposition 1 (Endogenous critical point). *Suppose*

1. $\beta(t)$ is asymptotically non-decreasing and $\liminf_{t \rightarrow \infty} \beta(t) > c_1 > 0$;
2. $\beta_c(t)$ is asymptotically non-increasing on average;
3. $\limsup_{t \rightarrow \infty} \beta_c(t) < c_1$.

Then $\beta(t)$ and $\beta_c(t)$ cross at some finite t^ ; at the crossing, the GMM’s symmetric state becomes unstable.*

The proof, given in Appendix B, is essentially a continuity argument: $\beta(t) - \beta_c(t)$ goes from $-|\beta(0) - \beta_c(0)| < 0$ (at $t=0$, before learning) to a strictly positive lim-inf, and must cross zero. The substantive content is in the hypotheses: (1) holds for any likelihood-maximizing GMM step, and (2) is the assertion that the encoder spreads the latent, which is the defining property of any information-preserving feature-learning objective. The novelty relative to Rose et al. [1990] is not the IVT step but the framing: β_c becomes a *time-dependent* observable that co-evolves with the encoder, turning the crossing event into a predictable training-time phenomenon rather than a static property of a frozen dataset.

3.5 Post-critical metastability: the bifurcation timing problem

Proposition 1 establishes that the crossing event $\beta(t^*) = \beta_c(t^*)$ exists; the symmetric state \mathcal{S}_0 becomes a saddle at t^* . The proposition is silent, however, on *when the broken-symmetry state becomes macroscopically observable*. The order parameter ε introduced in equation 5 obeys

$$\dot{\varepsilon} = (\beta - \beta_c)\varepsilon - \alpha\varepsilon^3 + \eta(t), \quad (7)$$

where $\eta(t)$ is a noise/dissipation term inherited from the encoder’s training dynamics. Just past the crossing, the unstable mode’s linear growth rate is $(\beta - \beta_c) \rightarrow 0^+$, so ε grows exponentially *from the noise scale* on a characteristic timescale that scales as $1/(\beta - \beta_c)$.

Remark 1 (Post-critical metastability). *The crossing event of Prop. 1 marks when \mathcal{S}_0 becomes unstable, not when the system reaches the broken-symmetry state. The lag between the two depends on the linear growth rate $(\beta - \beta_c)$ and the dissipation supplied by the encoder’s training dynamics. For continuously-driven objectives (e.g. contrastive losses), the lag is short and the post-critical descent in $(\log(\beta/\beta_c), \log \text{NC1})$ is observed immediately after the crossing. For under-dissipated objectives (e.g. supervised cross-entropy without explicit weight decay), the lag can extend over orders of magnitude in training steps, producing a long metastable plateau on which $\beta > \beta_c$ but NC1 has not yet collapsed. Section 4.2 presents an extreme empirical instance in which the crossing occurs within ~ 40 training steps but the macroscopic broken-symmetry transition is delayed by thousands of steps. Weight decay (the encoder’s most familiar dissipation knob) supplies the drift that ultimately triggers the transition, with the plateau length monotonically decreasing in WD and diverging as $\text{WD} \rightarrow 0$ at fixed noise scale. A control experiment with a 6-point WD sweep (Sec. 4.2, App. C) quantifies this empirically and shows the metastable plateau is a post-critical escape phenomenon, not a pre-bifurcation delay.*

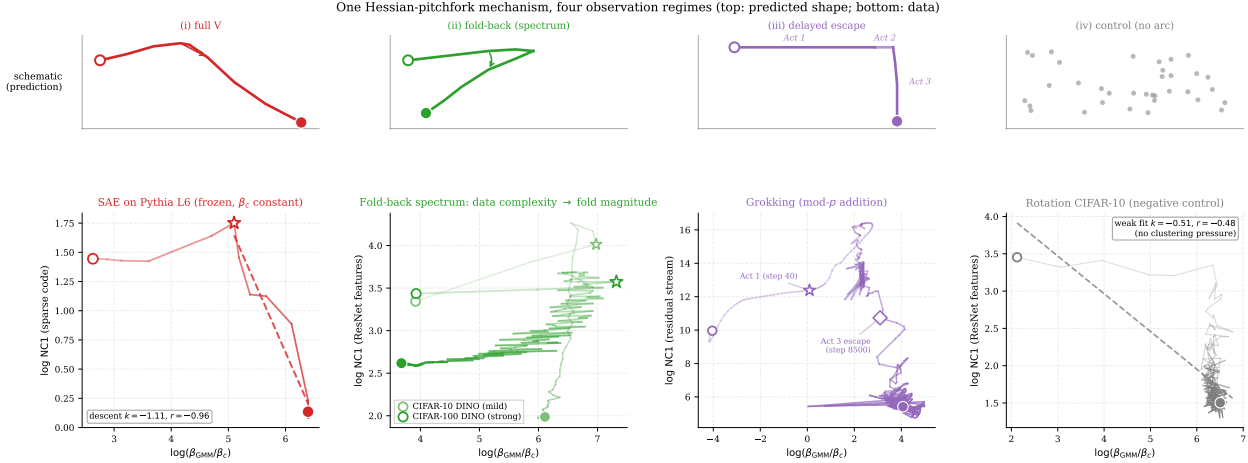


Figure 2: **Four observable shapes of the bifurcation arc, from the same Hessian-pitchfork mechanism.** Top row: schematic of each regime; bottom row: empirical realization. (i) *Full V* on SAE / frozen Pythia layer 6 (NC1 in sparse-code basis; star = V trough). (ii) *Fold-back spectrum* on DINO / CIFAR-10 (light green, mild) and CIFAR-100 (dark green, strong), fold magnitude controlled by data complexity. (iii) *Delayed escape* on grokking ($p = 97$, $WD = 1.0$; three-act structure detailed in Sec. 4.2). (iv) *No arc* on rotation-prediction (negative control). NC1 axes are not comparable across panels (sparse-code, backbone, residual-stream); the trajectory *shape* is the prediction. The 3-axis taxonomy explaining why exactly these four shapes appear is given in App. I.

4 The bifurcation arc across feature-learning methods

The Hessian-pitchfork prediction of Sec. 3 produces a three-phase trajectory in $(\log(\beta/\beta_c), \log \text{NC1})$ space: *pre-critical* ($\beta < \beta_c$, no class-aligned clustering, NC1 drifts slowly upward), *critical peak* ($\beta \approx \beta_c$, \mathcal{S}_0 becomes a saddle, NC1 peaks), *post-critical descent* ($\beta > \beta_c$, prototypes separate and $\log \text{NC1}$ falls linearly in $\log(\beta/\beta_c)$). The shape *observed in a particular setup* depends on (i) where the encoder begins ($\log(\beta/\beta_c) \leq 0$ at $t = 0$), (ii) the relative rates of $\beta(t)$ and $\beta_c(t)$ during training, and (iii) the dissipation rate (Remark 1). The combination yields four empirically distinguishable shapes: *full V* (frozen β_c ; one leg both ways), *fold-back* (β_c overtakes β post-onset, with magnitude controlled by data complexity; mild on CIFAR-10, strong on CIFAR-100), *delayed escape* (under-dissipated post-critical metastability, as in grokking), and *no arc* (negative control: no clustering pressure). We verify all four in two complementary experiments below.

4.1 Four shapes from feature-learning trajectories

We probe all four shapes here, across one sparse-coding-on-frozen-LM setup, two self-supervised setups (CIFAR-10 and CIFAR-100, illustrating the fold-back spectrum), one delayed-escape setup (grokking), and one negative control (rotation prediction), with a shared joint-detached GMM probe protocol ($K = 10$, $\text{lr}_\mu = 5 \times 10^{-3}$, $\text{lr}_\beta = 10^{-2}$, $\log \beta_0 = -2.5$; K_{probe} -robustness in App. K; full hyperparameter tables in App. M) so that $\beta_{\text{GMM}}(t)$ is directly comparable across methods. Figure 2 shows the four shapes; Table 1 reports the local descent slope k where applicable. The grokking panel of Fig. 2 shows a single canonical run for visual parity with the other panels; the full three-seed analysis with the three-act decomposition (Act 1 / Act 2 / Act 3 timing and WD -dependent escape time, with $\tau_{\text{esc}} \propto WD^{-1.23}$) is in Sec. 4.2 / Fig. 3.

(i) Full V. The SAE on Pythia-160M layer 6 freezes the upstream encoder, holding β_c constant. The entire motion in $\log(\beta/\beta_c)$ is driven by the SAE’s own precision growing past its critical point. NC1 (in the sparse-

Table 1: Trajectory shape across the six runs of Fig. 2, with the correlation r between $\log(\beta/\beta_c)$ and \log NC1 on the descent leg (after the V trough for SAE, after the fold-back peak for CIFAR-100 methods, on the full trajectory for already-supercritical CIFAR-10 methods and the control). The framework’s prediction across panels is *shape* and the *sign* of the post-critical relationship (negative when $\log(\beta/\beta_c)$ is rising along the descent leg, positive when it folds back). NC1 is computed in basis-specific normalizations (sparse code, ResNet features, residual stream), and the sample sizes n differ across runs, so neither $|r|$ nor the implicit slope magnitude is comparable across panels in a strict sense; we report r only to characterize the tightness of the relationship within each panel.

Method	Dataset	Shape	descent r	n
SAE on Pythia L6 ($K=2048$, soft-L1)	wikitext-103	(i) full V	-0.97	9
DINO C-100	CIFAR-100	(ii) fold-back (strong)	+0.90	278
SimCLR C-100	CIFAR-100	(ii) fold-back (strong)	+0.99	291
DINO C-10 (β_t)	CIFAR-10	(ii) fold-back (mild)	+0.96	50
SimCLR C-10	CIFAR-10	(ii) fold-back (mild)	+0.74	600
Rotation C-10	CIFAR-10	(iv) no arc (control)	-0.48	300

code basis, $K=2048$) rises slightly during pre-critical buildup, peaks, and then descends monotonically as predicted by the post-critical regime ($r = -0.97$, $n = 9$). The full V is visible because nothing competes for β_c . The SAE case is also the cleanest substrate for a deeper question (whether the bifurcation onset has *atom-level* mechanistic content beyond geometric coupling), which we take up in Section 5. App. G reports the complementary experiment of probing the LM’s hidden states directly without an intermediate SAE, showing why an SAE substrate is essential for the full V to be visible at all.

(ii) Fold-back (spectrum). When the encoder is itself learning a complex enough target, $\beta_c(t)$ may rise faster than $\beta(t)$ after the initial bifurcation, and the trajectory folds back left on the $\log(\beta/\beta_c)$ axis while NC1 continues to fall. The fold magnitude is controlled by data complexity. On CIFAR-100 (100 fine classes), both DINO and SimCLR exhibit *strong* fold-back: DINO peaks at $\log(\beta/\beta_c) = +7.09$ around epoch 35 and descends back to +3.68 by epoch 300 (~ 3 log-unit drift); SimCLR follows the same shape on a slightly compressed range. On CIFAR-10 (10 classes), ResNet-18 features begin already supercritical ($\log(\beta/\beta_c) \approx +3.9$ at random init) and the fold is *mild* (~ 0.5 log-unit leftward drift post-onset) for both DINO with native teacher-temperature β_t and SimCLR. The two datasets occupy the same kinematic regime; data complexity controls only the magnitude of β_c ’s post-onset rise.

(iii) Delayed escape. Under low dissipation, the system can sit on a post-critical metastable plateau for orders of magnitude in training steps before the macroscopic broken-symmetry transition fires (Remark 1). The grokking trace in Fig. 2 previews this; the three-act decomposition with multi-seed dissipation-threshold control is in Sec. 4.2.

(iv) No arc (negative control). Rotation prediction provides no clustering pressure, so the framework predicts no bifurcation. We see only weak scatter ($r = -0.48$, $n = 300$), with NC1 evolving largely independently of $\log(\beta/\beta_c)$ over a comparable range.

Sign of the post-critical relationship is kinematic. The relationship between $\log(\beta/\beta_c)$ and \log NC1 on the descent leg is negative when $\log(\beta/\beta_c)$ is rising on that leg (regime i, frozen β_c) and positive when it is falling or saturating (regime ii, fold-back). The framework does not predict a universal sign; it predicts an arc whose descent leg may be traversed in either direction in $\log(\beta/\beta_c)$ space depending on which of β or β_c moves faster.

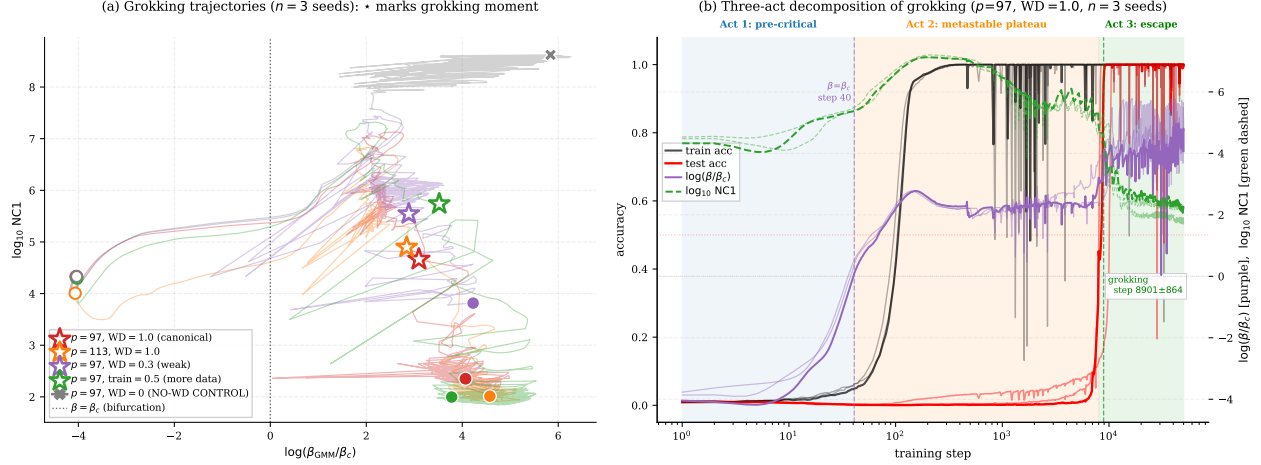


Figure 3: **Grokking decomposes into crossing, plateau, and escape.** (a) Trajectories of five grokking configurations ($n = 3$ seeds each, seed-0 trace shown) in $(\log(\beta/\beta_c), \log_{10} \text{NC1})$. \star marks the grokking moment (test acc > 0.5); \times marks the no-grok endpoint of the WD=0 control. (b) Canonical run ($p=97, \text{WD}=1.0, 3$ seeds overlaid), with the three acts highlighted as colored bands. *Act 1 (blue)*: β rapidly crosses β_c at step 37 ± 2 . *Act 2 (orange)*: a long metastable plateau in which $\log(\beta/\beta_c) \approx +3$ but $\log_{10} \text{NC1}$ sits at ≈ 6.7 ; the system is post-critical but the broken-symmetry order parameter is still microscopic. *Act 3 (green)*: at step $8\,900 \pm 864$, weight decay’s dissipation finally drives the order parameter off the saddle; NC1 collapses by four orders of magnitude over a few hundred steps and test accuracy jumps to 1.

4.2 Grokking: crossing, plateau, escape

The four SSL regimes share a feature: once β crosses β_c , the macroscopic broken-symmetry transition follows within at most a few epochs. Remark 1 predicts a fifth regime that decomposes into three distinct acts in training time:

- *Act 1: Crossing.* $\beta(t)$ crosses $\beta_c(t)$ and the symmetric state becomes a saddle.
- *Act 2: Metastable plateau.* The system is supercritical ($\beta > \beta_c$) but the order parameter ε has not yet grown to a macroscopic value; NC1 sits on a high plateau. The plateau length is set by the dissipation rate.
- *Act 3: Escape.* Dissipation (here, weight decay) finally drives ε off the saddle; NC1 collapses by orders of magnitude over a comparatively short window, and downstream test accuracy jumps from chance to ≈ 1 . This is the grokking transition.

The previous reading of grokking, “the model suddenly acquires generalization at some moment,” is misleading; the model becomes *eligible* to acquire it within the first ~ 40 steps and then spends thousands of steps trying to escape a saddle. Grokking on modular arithmetic is the cleanest empirical realization of this three-act picture.

Setup. Following Nanda et al. [2023], we train a 1-layer transformer ($d_{\text{model}} = 128, 4$ heads, $d_{\text{mlp}} = 512$) on $a + b \bmod p$ tokens with AdamW, $\text{lr} = 10^{-3}$, full-batch gradient descent, 30% train fraction. The probe is the same joint-detached protocol of Sec. 4.1, attached to the residual stream at the = position; β_c is computed from $\text{Cov}(z)$ on the test set, NC1 is computed against the p output classes. Three seeds per configuration.

Act 1: the crossing is fast and universal. Across all 15 runs (5 configs \times 3 seeds), $\log(\beta/\beta_c)$ crosses zero in the first 34–60 training steps (Table 2). The crossing event is tight ($\sigma \approx 2$ steps within each configuration)

Table 2: Grokking experiments, mean \pm std across $n = 3$ seeds. Act 1 (the $\beta = \beta_c$ crossing) is universal and tight ($\sigma \approx 2$); Act 3 escape time spans more than an order of magnitude in WD. Full WD sweep at the 200,000-step horizon is in Table 3; the WD=0 control fails to escape within 50,000 steps in all 3/3 seeds.

Config	Memo	Act 1: $\beta = \beta_c$	Act 3: grok	Final $\log(\beta/\beta_c)$	n_{grok}
$p=97$, WD=1.0 (canonical)	253 ± 6	37 ± 2	$8\,900 \pm 864$	$+4.49 \pm 0.47$	3/3
$p=113$, WD=1.0	297 ± 49	39 ± 2	$6\,633 \pm 1\,461$	$+4.88 \pm 0.45$	3/3
$p=97$, WD=0.3 (weak)	263 ± 2	36 ± 2	$38\,150 \pm 4\,250$	$+4.07 \pm 0.46$	3/3
$p=97$, train=0.5	242 ± 52	54 ± 6	$1\,250 \pm 398$	$+4.45 \pm 0.54$	3/3
$p=97$, WD=0 (control)	273 ± 8	36 ± 2	never	$+6.07 \pm 0.17$	0/3

and reached in *every* seed of *every* configuration, including the no-grok WD=0 control. This is the Hessian-pitchfork prediction of Sec. 3 in raw form: the supercriticality condition $\beta > \beta_c$ is universally met within the first few steps of training.

Act 2: the plateau is the post-critical metastable saddle. For thousands of steps after the crossing, $\log(\beta/\beta_c)$ continues to rise toward $\sim +4$ but NC1 does not move from its high plateau. The previous (and incorrect) reading would call this an undertrained representation. The framework’s reading (Remark 1) is sharper: the encoder is parked near $\varepsilon = 0$ on a saddle that is *linearly* unstable but whose exit time is set by noise and dissipation. The plateau length is the dissipation-controlled escape time, not a pre-bifurcation delay.

Act 3: escape is dissipation-controlled. At sufficiently long horizon (200,000 steps), all configurations with WD > 0 escape in 3/3 seeds, but the escape time is strongly monotonic in WD: τ_{esc} rises from 8 900 steps at WD=1.0 to 147 167 steps at WD=0.1, while WD=0 fails to escape in 0/3 seeds within 50,000 steps. The full sweep fits a power-law $\tau_{\text{esc}} \propto \text{WD}^{-1.23}$ ($\Delta\text{AIC} = +19.3$ over the Kramers form equation 15; Table 3, App. C). The WD=0 control reaches $\log(\beta/\beta_c) = +6.07$, higher than any grokked run, yet NC1 grows to $\sim 10^8$ and test accuracy stays at ~ 0.01 in all three seeds; the metastable plateau is a saddle that requires dissipation to escape. Beyond the weight-decay axis, escape time also scales predictably with the modulus p and the training fraction (Table 2). At escape, \log_{10} NC1 drops from ≈ 6.7 to ≈ 2.4 over a few hundred training steps while $\log(\beta/\beta_c)$ moves by less than 1 log-unit; the entire post-critical descent shape of Sec. 4.1 is compressed into this narrow window.

Control experiment: WD-controlled metastable plateau length. The grokking setup is unusual in giving us a single, clean dissipation knob (WD) that is otherwise neutral with respect to the Hessian-pitchfork mechanism: changing WD does not shift Act 1 (the crossing remains at step 36–37 across all WD; cf. $\beta = \beta_c$ column of Table 2) and does not change the post-critical $\log(\beta/\beta_c)$ trajectory shape, only its *rate*. This lets us treat the WD sweep as a control experiment for Remark 1: if the metastable plateau is genuinely a post-critical escape phenomenon, then dialing the encoder’s dissipation should monotonically change the plateau length, and at zero dissipation the system should stay on the plateau indefinitely. We measure τ_{esc} at six WD levels $\gamma \in \{0.1, 0.2, 0.3, 0.5, 0.7, 1.0\}$ with $n = 3$ seeds per level and a 200,000-step horizon long enough to observe escape at every $\gamma > 0$ (Table 3).

The result is unambiguous on the qualitative claim: τ_{esc} is monotonically decreasing in γ across two decades of plateau lengths (8.9k \rightarrow 147k steps), and the $\gamma = 0$ control fails to escape in any of 3 seeds within 50k steps despite reaching $\log(\beta/\beta_c) = +6.07$. This directly supports Remark 1: the crossing event makes the symmetric state unstable, but the macroscopic broken-symmetry transition is a dissipation-controlled post-critical escape, not an immediate consequence of the crossing.

On the quantitative form, the 6-point fit prefers a power-law $\tau \propto \gamma^{-1.23}$ over an exponential (activation-dominated Kramers) form $\tau \propto e^{-\kappa\gamma/D}$ *decisively*: $\Delta\text{AIC} = +19.3$, power-law residuals within $\sim 10\%$

Table 3: WD-intervention control experiment: escape times at $p = 97$, train fraction 0.3, $n = 3$ seeds per WD, 200,000-step horizon. Power-law fit $\tau \propto \gamma^{-1.23}$ is within $\sim 10\%$ at every WD; activation-dominated Kramers form is decisively ruled out ($\Delta\text{AIC} = +19.3$; see App. C).

γ (WD)	τ_{esc} (steps, observed)	τ_{esc} (power-law fit)	escape rate
0.0	∞ (no escape in 50k)	∞	0/3
0.1	$147\,167 \pm 23\,618$	151 987	3/3
0.2	$88\,033 \pm 27\,091$	65 006	3/3
0.3	$38\,150 \pm 4\,250$	39 554	3/3
0.5	$22\,433 \pm 6\,064$	21 152	3/3
0.7	$16\,633 \pm 5\,008$	14 006	3/3
1.0	$8\,900 \pm 864$	9 047	3/3

at every WD, Kramers under-predicts the weak-dissipation escape times by $\sim 1.7\times$ at WD= 0.1. We treat this as an empirical characterization specific to the modular-arithmetic grokking setup rather than a theoretical prediction of the bifurcation framework; the regime-selection analysis (drift-dominated vs. activation-dominated post-critical escape) is in App. C.

Predictive content of the indicator. At any training step during a grokking run, $\log(\beta/\beta_c)$ identifies the system’s current act: pre-critical (Act 1, $\log(\beta/\beta_c) < 0$), post-critical metastable (Act 2, $\log(\beta/\beta_c) > 0$ with NC1 on the plateau), or escaping (Act 3, NC1 descending). At step 100 of the canonical run, $\log(\beta/\beta_c) = +3$ already places the system in Act 2: the trajectory has become *eligible to grok*, $\sim 8\,400$ training steps before test accuracy provides any signal. Combined with the dissipation strength of the encoder (a known hyperparameter), the indicator predicts both whether grokking will occur (no escape at WD=0, Tab. 2) and roughly when ($\tau_{\text{esc}} \propto \text{WD}^{-1.23}$, spanning 8 900 steps at WD=1.0 to 147 167 at WD=0.1; Tab. 3). This is prediction in the operational sense: from the indicator and the dissipation strength, both readable at step 100, the trajectory’s downstream state is forecastable orders of magnitude before test_acc, train_acc, or the training loss show any sign of the transition.

4.3 Synthesis

A single Hessian-pitchfork prediction is governed by three binary kinematic axes (initial sub/supercriticality, post-onset β -vs- β_c kinematics, dissipation rate; Appendix I). The axes predict which kinematic regimes are accessible to which classes of feature-learning pipelines: standard SSL methods on rich datasets occupy the fold-back regime, frozen-encoder SAE training traces a full V, under-dissipated supervised settings exhibit delayed escape, and clustering-pressure-free objectives produce no arc. We observe all four regimes in the corresponding settings; the remaining nominal axis combinations are either degenerate or unreached by standard pipelines. Method-specific differences (in fold-back magnitude, plateau length, and descent shape) are kinematic consequences of the encoder–probe race and of the encoder’s dissipation, not methodology-specific physics. In particular, the visual difference between CIFAR-10 (mild fold, ~ 0.5 log-unit leftward drift) and CIFAR-100 (strong fold, ~ 3 log-units) is a magnitude difference within the same fold-back regime, controlled by data complexity (number of classes \rightarrow richer post-critical $\text{Cov}(z)$ structure \rightarrow larger β_c rise). The quantity $\log(\beta(t)/\beta_c(t))$, computed from the encoder’s hidden state and a passive GMM probe alone, is the label-free indicator of where in the arc a given run currently sits.

The arc-level results above confirm the theory at the *trajectory* level. We now turn to its sharpest empirical consequence at the *per-atom* level: the SAE feature lottery (Section 5).

5 The first 5% of SAE training is a feature lottery: testing the per-atom prediction

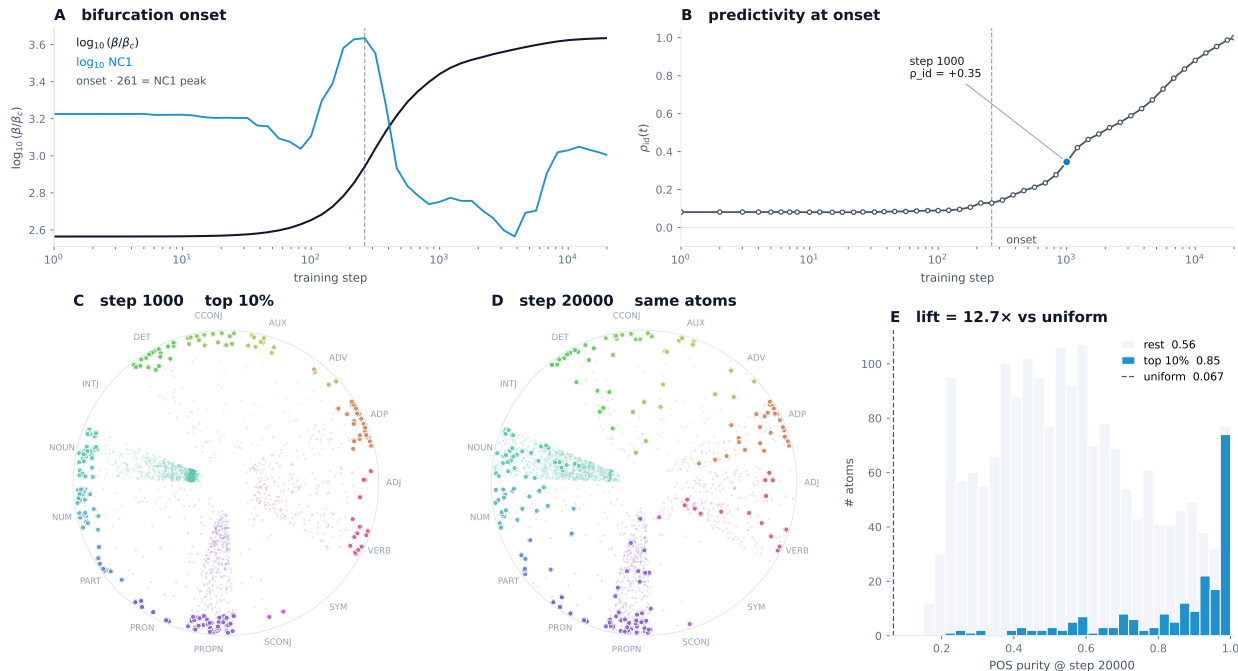


Figure 4: SAE feature lottery emerges at the bifurcation onset and is operationally selectable by 5% of training. ($K = 2048$ top- K SAE on Pythia-160M layer 6; one canonical seed shown, 3-seed statistics quoted.) (A) Onset: $\log_{10}(\beta_{\text{SAE}}/\beta_c)$ (black) crosses zero and rises; $\log_{10} \text{NC1}_{\text{features}}$ (blue) peaks at step 261, our operational definition of onset. (B) Per-atom predictivity: cross-atom Spearman $\rho_{\text{id}}(t)$ of POS purity at t vs convergence sits at noise floor pre-onset, climbs sharply at the bifurcation, reaches $+0.41 \pm 0.04$ at step 1,000 ($+0.35$ in shown seed). (C) Top decile of atoms by step-1,000 POS purity ($n = 205$ of 1843 active), placed at the angular sector defined by their dominant POS class; radius = step-1,000 purity. (D) Same atoms, same sectors, radius now = step-20,000 purity: the outer-ring population persists in every major POS sector; bulk inward drift reflects sparsity tightening, not specialization loss. (E) Top decile reaches POS purity 0.82 ± 0.03 at convergence (3 seeds: 0.80/0.86/0.82), $12.3 \pm 0.4 \times$ the uniform-random baseline. Reports POS-purity persistence, not POS-class identity preservation.

Sections 3–4 establish that the bifurcation onset is a *collective* event: the encoder’s symmetric collapsed state loses stability at a specific moment, with an unstable subspace shared by all $K - 1$ anti-symmetric modes (App. A.2). The theory therefore makes a sharp *per-atom* prediction: at the bifurcation, each atom must select a specific direction from this shared manifold, and that selection should be detectable as an atom-level identity event in training time. This section tests that prediction in the cleanest available substrate.

Among the four regimes catalogued in Sec. 4, the SAE on frozen Pythia-160M layer 6 is the only setting in which β_c is constant by construction; the upstream encoder does not evolve. This makes it the cleanest substrate to disentangle the bifurcation event (shared by both SAE families we tested) from *per-feature* interpretability (architecture-dependent). It is also the natural substrate for studying the crossing event in language models at all: raw LM activations are heavily anisotropic (Pythia-160M layer 6 has $\lambda_{\max}(\text{Cov}(z))/\bar{\sigma}^2 \approx 380$), so a randomly initialized GMM probe attached directly to LM hidden states starts already supercritical and never visibly crosses β_c . The SAE itself, by contrast, initializes with low β_{SAE} and

grows past a fresh critical point, making the full pre-/post-critical arc observable in the sparse-code basis. We train two SAE families on the same Pythia activations with dictionary size $K = 2048$ over input dimension $d = 768$: (i) **soft-L1** (ReLU activation, L_1 penalty on activations, $\lambda \in \{5 \times 10^{-4}, 2 \times 10^{-3}, 5 \times 10^{-3}, 10^{-2}\}$) and (ii) **top- K** (hard architectural sparsity with $\text{top}_k = 64$ active atoms per token, following Gao et al. 2025). Both are trained for 20,000 steps with identical optimizer, batch size, and dense (~ 55 -point) checkpoint schedules.

We find a sharp dynamical phase transition: per-atom predictive content goes from zero pre-onset to substantial within the first 5% of training, and atoms ranked at 5% already recover the highest-purity atoms at convergence. Following Frankle and Carbin [2019], we refer to this as a *feature lottery*; the drawing event is the first phase transition during training, not initialization. The lottery is the theory’s sharpest empirical confirmation; the detailed quantitative results follow.

Per-atom identity. For each saved checkpoint we forward a fixed POS-labeled WikiText-103 eval set ($N = 50,000$ tokens) through the SAE to obtain feature activations $f \in \mathbb{R}^{N \times K}$. Atom k ’s *activation-pattern identity* is the column $f_{:,k} \in \mathbb{R}^N$; two atoms have the same identity when their N -dimensional activation vectors are cosine-close. This substrate is invariant to atom permutation and scaling, and bypasses the geometric near-saturation of decoder-column matching that arises in overcomplete dictionaries ($K > d$, App. J).

5.1 The lottery is selectable by 5% of training

The cross-atom $\rho_{\text{id}}(t)$ trajectory plotted in Fig. 4B is constructed by *identity matching*: atom k at step t is compared to atom k at step 20,000, with no cross-time atom permutation (an alternative Hungarian-matched ρ_H is artifact-inflated; see “Why not Hungarian” below). Values at representative checkpoints:

step	ρ_{id}	interpretation
46	+0.03	noise floor, atoms have no identity
178	+0.06	still noise floor
261	+0.16	bifurcation onset; lottery begins
464	+0.31	post-critical descent
1,000	+0.41	5% of training; useful early-ranking signal acquired
2,154	+0.49	slow refinement
10,000	+0.88	
20,000	+1.00	anchor (self-comparison)

Two caveats beyond what Fig. 4 shows:

1. *Pre-onset ρ_{id} is statistically indistinguishable from 0 for $t < 200$, confirming atoms have no detectable identity before the bifurcation.*
2. *The lottery is operationally useful at 5%, but identity refinement continues.* The remaining 95% of training lifts ρ_{id} from 0.41 to 0.88. We therefore do not claim the lottery is “complete” at 5% in the strong sense of Frankle and Carbin [2019] (where identification at initialization is followed by isolated retraining to full accuracy). Ours is the weaker statement that early ranking provides a useful predictor of converged identity.

This is the SAE-level analogue of the lottery-ticket framing of Frankle and Carbin [2019]: where they show that winning subnetworks are selectable at initialization in supervised classifiers, we find that winning SAE atoms are selectable at the first phase transition of unsupervised dictionary training. The bifurcation onset is the lottery’s drawing event.

Ranking lift (three seeds). At convergence, the decile of atoms ranked by their step-1,000 POS purity has mean POS purity 0.82 ± 0.03 (mean \pm std across $n = 3$ seeds; seed 0 / 1 / 2 give 0.80 / 0.86 / 0.82) versus 0.47 ± 0.03 for the bottom decile. The relevant null for the lottery claim — “does step-1,000 ranking carry predictive content for convergence identity?” — is uniform-random selection, under which top-decile mean equals the corpus POS-class prior $1/15 \approx 0.067$ (the 15 POS classes in the WikiText eval set). Early-screened top-decile atoms achieve $12.3 \pm 0.4\times$ this uniform-random baseline. The identity-matched Spearman across the three seeds is $\rho_{\text{id}} = +0.41 \pm 0.04$, all $p < 10^{-80}$. The corresponding single-seed numbers for the soft-L1 SAE are 0.64 (top decile) versus 0.35 (bottom decile), $10\times$ uniform-random baseline. Both architectures support the same conclusion: **early winner screening at 5% of training is feasible and identifies a substantial fraction of the highest-purity atoms**, though full training is still required to obtain each atom’s highest-quality final activations.

Architecture invariance. The same ρ_{id} trajectory and 5% cutoff are recovered in soft-L1 SAEs (ReLU activation, L_1 penalty $\lambda \in \{5 \times 10^{-4}, 2 \times 10^{-3}, 5 \times 10^{-3}, 10^{-2}\}$, $L_0 \approx 1000$ of $K = 2048$) despite their different sparsity regime: the post-critical descent of ρ_{id} is qualitatively identical (App. J), demonstrating that the lottery is a property of the bifurcation, not of the architectural top- K mask.

Why ρ_{id} and not ρ_H (Hungarian). We initially considered Hungarian-matched correlation ρ_H ; match atoms across time by maximizing cosine of activation patterns, then correlate matched pairs’ POS purities. This metric is systematically inflated: at random initialization (step 46, where atoms have no identity by construction), $\rho_H \approx 0.30$ rather than 0 (App. L, panels D–E). The inflation arises because Hungarian matching preferentially pairs atoms with similar activation profiles, and POS purity is itself computed from the activation profile, so high-purity atoms find each other across time even when no underlying identity is preserved. Subtracting the 0.30 floor recovers the ρ_{id} trajectory. ρ_{id} , which is invariant to this confound, is the estimator we report throughout.

Specificity. Of three per-atom early metrics tested, only POS purity carries the predictive signal:

- *Early POS purity* \rightarrow final POS purity: $\rho_{\text{id}} = +0.41$ at 5%. **Predictive.**
- *Early activation concentration* \rightarrow final POS purity: $\rho \approx 0$ in the top- K SAE, $\rho \approx -0.28$ in the soft-L1 SAE. **Not predictive.**
- *Early identity-lock cosine* \rightarrow final POS purity: $\rho = +0.20$ (top- K). Weakly predictive.

This specificity rules out the trivial reading “any atom-level property predicts its convergence value.” What is drawn at the bifurcation is specifically *linguistic identity*, not generic firing strength or generic stability.

5.2 Mechanism: identity lock during the lottery window

Why is the lottery permanent past 5% of training? Atom identities themselves lock during the post-critical window. The Hungarian-matched cosine between per-atom activations at step t and at the converged SAE remains flat (at random baseline 0.13 for top- K , 0.68 for soft-L1) for $t < 200$, begins a sharp rise at the NC1 peak (step 261 for top- K , 383 for soft-L1), and saturates at 1.0 by step $\sim 15,000$. Both SAE families share this timing; only their random-init baselines differ (soft-L1’s ReLU rows already project onto the data subspace). The onset is therefore the *trigger* of a per-atom assignment process: each atom commits to a specific activation pattern during the post-critical window, and subsequent training refines but does not reshuffle that commitment (App. L, Fig. 17).

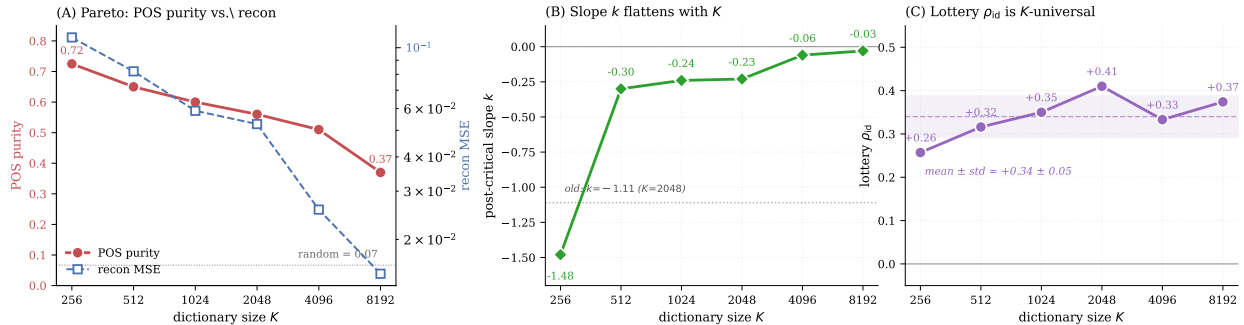


Figure 5: **K-sweep across $K \in \{256, 512, 1024, 2048, 4096, 8192\}$ at fixed 3% top- K sparsity.** For each K , we report final L_0 , final reconstruction MSE, the lottery Spearman ρ_{id} , and the mean POS purity of the top-decile atoms ranked by step-1,000 POS purity. Universality across K : the lottery $\rho_{id} \in [+0.26, +0.41]$ is K -stable and consistently positive: the bifurcation onset is a K -universal event. Monotonicity in K : POS purity *decreases* with K (0.725 at $K = 256$, 0.370 at $K = 8192$), while reconstruction MSE decreases the other way.

5.3 Architecture-dependent ceiling on feature interpretability

The bifurcation event is shared by both SAE families we tested, but the *post-onset ceiling* on per-feature interpretability is not. Under architectural top- K sparsity, the median active feature reaches POS purity 0.56 ($8\times$ random); the soft-L1 family plateaus at 0.33, since L_0 saturates near 1,000 of $K = 2048$ irrespective of $\lambda \in [5 \times 10^{-4}, 10^{-2}]$. The bifurcation locks identities identically in both families; only top- K pushes those identities into linguistically selective directions. Who wins the lottery is determined at the bifurcation; how linguistically meaningful the winning identity is depends on the post-onset sparsity regime (App. L).

5.4 K-sweep: universality of the lottery, monotonicity of interpretability and slope

We sweep $K \in \{256, 512, 1024, 2048, 4096, 8192\}$ at fixed top- K sparsity ratio of 3% (so top_k scales proportionally as $\{8, 16, 32, 64, 128, 256\}$) with all other hyperparameters held constant. The K -stability of ρ_{id} visible in Fig. 5 is statistically tight ($p < 10^{-3}$ at every K), justifying treating the bifurcation onset as a K -universal event.

POS purity is monotonically decreasing in K , but K -confounded. The median atom’s POS purity at convergence falls steadily from 0.725 at $K = 256$ to 0.370 at $K = 8192$ (Table 4). The mechanism is that a smaller dictionary forces each atom to absorb a coarser token-cluster partition that more easily aligns with the 15-way POS partition; a larger dictionary spreads across finer sub-categories that POS purity is too coarse to resolve. We emphasize that this trend is therefore *partly a structural property* of POS purity as a metric, not a direct statement that small K produces more mechanistically interpretable features: a K -unbiased interpretability metric (causal mediation, LLM-as-judge) is required before a Pareto-based recommendation can be made.

Pareto frontier, with a K -bias caveat. $K = 256$ scores higher on POS purity; large K scores better on reconstruction. The framework adds a second axis (atom-level POS purity, plus the lottery ρ_{id}) to the standard SAE L_0 -vs-recon Pareto. However, because POS has only 15 classes, the POS-purity-vs- K trend is partly a structural artifact: smaller K forces each atom to absorb a coarser token-cluster partition, which more easily aligns with a 15-way categorical metric. We therefore do *not* recommend small K on the basis of

Table 4: K-sweep at fixed top- K sparsity ratio 3%, all other hyperparameters constant. The lottery ρ_{id} is K -stable; POS purity decreases monotonically with K while reconstruction MSE decreases the other way.

K	L_0	recon MSE	POS purity (median atom)	ρ_{id} (lottery)
256	8	1.09×10^{-1}	0.725	+0.26
512	16	8.20×10^{-2}	0.650	+0.32
1024	32	5.89×10^{-2}	0.600	+0.35
2048	64	5.27×10^{-2}	0.560	$+0.41 \pm 0.04$ ($n=3$)
4096	128	2.57×10^{-2}	0.510	+0.33
8192	256	1.50×10^{-2}	0.370	+0.37

POS purity alone; a K -unbiased interpretability metric (such as causal mediation [cf. Nanda et al., 2023] or LLM-as-judge scoring) is required before a substantive recommendation can be made. What is robust to this caveat is the K -universal lottery effect: at every $K \in \{256, \dots, 8192\}$, atom-level identity is predictable from 5% training with $\rho_{\text{id}} \in [+0.26, +0.41]$.

5.5 Connection to the bifurcation theory

The pitchfork bifurcation and the feature lottery are two scales of the same event. At $\beta = \beta_c$ the unstable subspace is shared by all $K-1$ anti-symmetric modes (App. A.2); each atom selects a specific direction from this manifold via random initialization noise and the cubic terms in equation 5. The collective bifurcation enables the per-atom selection; the per-atom selection is what makes post-onset identities permanent and partially predictable. The following proposition formalizes the per-atom directional preservation that the empirical $\rho_{\text{id}} > 0$ (Sec. 5.1) realizes.

Proposition 2 (Per-atom directional persistence). *Consider the coupled order-parameter dynamics on the $(K-1)$ -fold-degenerate unstable subspace just past the crossing ($\mu := \beta - \beta_c > 0$, small),*

$$\dot{\epsilon}_k = \mu \epsilon_k - \alpha \|\epsilon_k\|^2 \epsilon_k - \gamma \sum_{j \neq k} (\epsilon_j^\top \epsilon_k) \epsilon_j + \eta_k(t), \quad k = 1, \dots, K, \quad (8)$$

with i.i.d. Langevin noises η_k at intensity D and cubic inter-mode coupling strength $\gamma \geq 0$. Assume each initial perturbation satisfies $\|\epsilon_k(0)\| > \sigma_* \sqrt{D/\mu}$ for some $\sigma_* > 1$ (initial perturbation above the noise floor). Then in the weak-coupling regime $\gamma \ll \alpha$, for any finite time T within the post-saturation, pre-randomization window $\tau_r \lesssim T \ll T_{\text{rand}} := r^{*2}/(2(d-1)D)$ (where τ_r is the deterministic radial saturation timescale and T_{rand} is the spherical randomization timescale on the saturated attractor), the per-atom directional persistence is strictly positive:

$$\mathbb{E}[d_k(0)^\top d_k(T)] > 0, \quad d_k(t) := \epsilon_k(t)/\|\epsilon_k(t)\| \in S^{d-1}, \quad (9)$$

with magnitude controlled by $\sigma_* \mu/(\alpha D)^{1/2}$ and expectation taken over the Langevin noise realizations. For training runs of fixed horizon, T is the training time; in the strict $T \rightarrow \infty$ limit, angular Brownian motion on the saturated sphere eventually randomizes $d_k(T)$ and the persistence claim breaks down (outside the scope of this proposition).

Proof sketch (full proof in App. D). At $\gamma = 0$, modes decouple. Each ϵ_k obeys an independent pitchfork SDE whose deterministic flow is *radial*: the linear growth $\mu \epsilon_k$ preserves direction, and the cubic self-saturation $-\alpha \|\epsilon_k\|^2 \epsilon_k$ also preserves direction. Noise rotates direction with effective diffusion coefficient $(d-1)D/\|\epsilon_k\|^2$, which decays rapidly as $\|\epsilon_k\|$ grows from $\sigma_* \sqrt{D/\mu}$ toward $\sqrt{\mu/\alpha}$. Over the finite window $[0, T]$, the accumulated angular variance is $\Theta^2(T) \approx (d-1)/\sigma_*^2 + 2(d-1)D(T - \tau_r)/r^{*2}$, which is $O(1/\sigma_*^2)$ as long as the saturation-phase contribution $(T - \tau_r)/T_{\text{rand}}$ is sub-leading. For small $\Theta(T)$,

β/β_c as label-free diagnostic: DINO from scratch, 5 modes (exp 19, CIFAR-10)

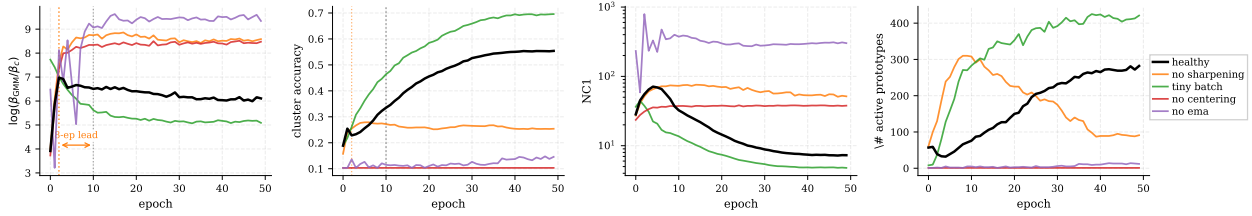


Figure 6: **From-scratch DINO with four perturbed modes** ($n = 1$ seed per mode). Healthy (black) versus four perturbations over 50 epochs of CIFAR-10 training. The two perturbations relevant for the diagnostic claim are *no_sharpening* (orange) and *tiny_batch* (green): both separate from healthy in $\log(\beta/\beta_c)$ at epoch 2 (vertical dotted line) while cluster accuracy diverges only by epoch 10, an ~ 8 -epoch lead time. The two outcomes go in opposite directions; *no_sharpening* degrades ($\sim 25\%$ cluster accuracy at epoch 50 vs $\sim 55\%$ healthy); *tiny_batch* improves ($\sim 70\%$). The catastrophic modes (*no_centering*, *no_ema*) collapse from initialization and provide no epoch-resolution lead-time signal.

$\mathbb{E}[d_k(0)^\top d_k(T)] \approx 1 - \Theta^2(T)/2 > 0$. Adding weak inter-mode coupling $\gamma > 0$ contributes an $O(\gamma/\alpha)$ perturbation that preserves the sign of $\mathbb{E}[d_k(0)^\top d_k(T)]$ at leading order, since the coupling vanishes when modes are mutually orthogonal (and modes self-orthogonalize under the cubic saturation). \square \square

Empirical proxies for per-atom persistence. Equation 9 is per-atom: at finite T within the persistence window, each atom’s direction positively correlates with its direction at the bifurcation onset. We do not have direct access to $d_k(T)^\top d_k(0)$ in real SAEs (the unstable manifold is not explicitly parameterized); we use the following two empirically accessible proxies, both of which inherit positivity from equation 9 under the same regime assumption.

Scalar-projection proxy (toy verification, App. D.3, Fig. 8). Fix a reference direction $r \in S^{d-1}$ and consider the per-atom scalar autocorrelation $A_k(T) := \langle \varepsilon_k(0), r \rangle \cdot \langle \varepsilon_k(T), r \rangle / (\|\varepsilon_k(0)\| \|\varepsilon_k(T)\|)$. By equation 9, $\mathbb{E}[A_k(T)] > 0$ for each k . Across K i.i.d. atoms, the Spearman correlation between the projection pair $(\langle \varepsilon_k(0), r \rangle, \langle \varepsilon_k(T), r \rangle)$ converges to a positive population Spearman as $K \rightarrow \infty$; direct SDE simulation in App. D.3 confirms $\rho = 0.948 \pm 0.006$ across 5 seeds.

POS-purity proxy (SAE empirics, Sec. 5.1). Per-atom POS purity is the magnitude of an atom’s projection onto a linguistic POS subspace of \mathbb{R}^N . Under equation 9, this projection is per-atom-autocorrelated across training time: the early-time and late-time POS purity for the same atom are positively correlated. The identity-matched Spearman $\rho_{\text{id}} = 0.41 \pm 0.03$ across atoms (Sec. 5.1) is the population Spearman of this per-atom autocorrelation; the positive sign is equation 9’s prediction, the specific magnitude (+0.41) depends on the linguistic geometry of POS classes in Pythia’s residual stream and is not predicted by the theory.

5.6 Scope and limitations

The lottery claim is bounded along three axes. (i) *POS purity is one interpretability dimension*: atoms detecting finer structure (named entities, sub-POS, phrase patterns) may be mechanistically interpretable without scoring high on POS purity; our claim concerns the POS-selective subset only. (ii) *Secondary bifurcations*. The hierarchical structure (Sec. 3) predicts that finer features should themselves exhibit phase transitions at $\beta_c^{(2)} = 1/\lambda_{\max}(\Sigma_{\text{within}})$ later in training; verification at the secondary scale is left to future work. (iii) *Tagger noise*. spaCy [Honnibal et al., 2020] reports $\sim 97\%$ POS accuracy on standard benchmarks, with errors concentrated on ambiguous cases (gerunds, deverbal nouns); reported ρ_{id} values are therefore conservative lower bounds on true atom-level POS selectivity.

Frequency-confound check. A natural concern is that the lottery effect is inflated by token frequency: atoms that lock onto a single high-frequency token (e.g. “the”) would achieve high POS purity trivially, since high-frequency function words have stable POS tags. To rule this out, we stratify atoms by the mean log-frequency of their top-100 activating tokens into five quintiles and re-compute ρ_{id} within each quintile (3 seeds, $K = 2048$ top- K SAE). The result (Tab. 5, Fig. 18): all five quintiles show $\rho_{\text{id}} \in [+0.37, +0.51]$, well above zero ($p < 10^{-3}$ each), with no monotonic increase from rare to frequent tokens. The frequency confound is not load-bearing.

Table 5: ρ_{id} stratified by atom top-100-token mean log-frequency, 3 seeds, $K = 2048$. Unstratified $\rho_{\text{id}} = +0.416 \pm 0.010$. The quintile range $[+0.37, +0.51]$ is small compared to the overall effect over the random baseline ($\rho = 0$), and Q4 (mid-frequency content words) rather than Q5 (most frequent function words) has the highest ρ_{id} , opposite to what a single-token-lock artifact would predict.

quintile of atom top-token mean log-freq	ρ_{id}
Q1 (rarest tokens)	$+0.368 \pm 0.034$
Q2	$+0.373 \pm 0.020$
Q3	$+0.365 \pm 0.025$
Q4	$+0.512 \pm 0.029$
Q5 (most frequent)	$+0.424 \pm 0.026$

6 Label-free training diagnostic in practice

The phase-identification ability documented in Sec. 4.2 (that β/β_c reads the encoder’s current act from its hidden state alone, well before downstream metrics respond) generalizes beyond grokking. We now test the same property in a more typical training-health setting: detecting the onset of representation degradation in a self-supervised encoder. The bifurcation framework predicts that β/β_c tracks representation-level state. We now ask whether this is operationally useful as a label-free training health indicator: does β/β_c respond earlier than downstream metrics when training drifts away from a healthy trajectory? We test this in two complementary setups: DINO trained from scratch with collapse modes injected at initialization (Sec. 6.1), and DINO with interventions applied to a healthy mid-training checkpoint (Sec. 6.2).

6.1 From-scratch collapse modes

We train ResNet-18 + DINO on CIFAR-10 for 50 epochs in five configurations (Fig. 6): healthy; *no_centering* (no center-buffer update on teacher logits); *no_sharpening* (teacher temperature pinned to student temperature); *no_ema* (teacher copies student each step); *tiny_batch* (batch size 32 instead of 256).

The two non-catastrophic perturbations (*no_sharpening*, *tiny_batch*) probe the diagnostic in opposite directions:

Negative case (*no_sharpening*). $\log(\beta/\beta_c)$ crosses the 0.5-log-unit deviation threshold from healthy at epoch 2 while cluster accuracy crosses the 5%-deviation threshold only at epoch 10: **an ~ 8 -epoch lead time on a 50-epoch run**, with the downstream outcome being degradation (25% vs 55% at epoch 50).

Positive case (*tiny_batch*). A non-catastrophic perturbation (batch 32 vs 256) where $\log(\beta/\beta_c)$ also separates from healthy by ~ 0.5 log-units at epoch 2, while the training-loss difference at that point is within batch noise. By epoch 50, cluster accuracy has separated by 15 percentage points in the *opposite* direction (70% *tiny_batch* vs 55% healthy). The early β/β_c separation thus predicts the downstream divergence with ~ 48 -epoch lead time; and the divergence is positive, not negative. Together with *no_sharpening*, this shows

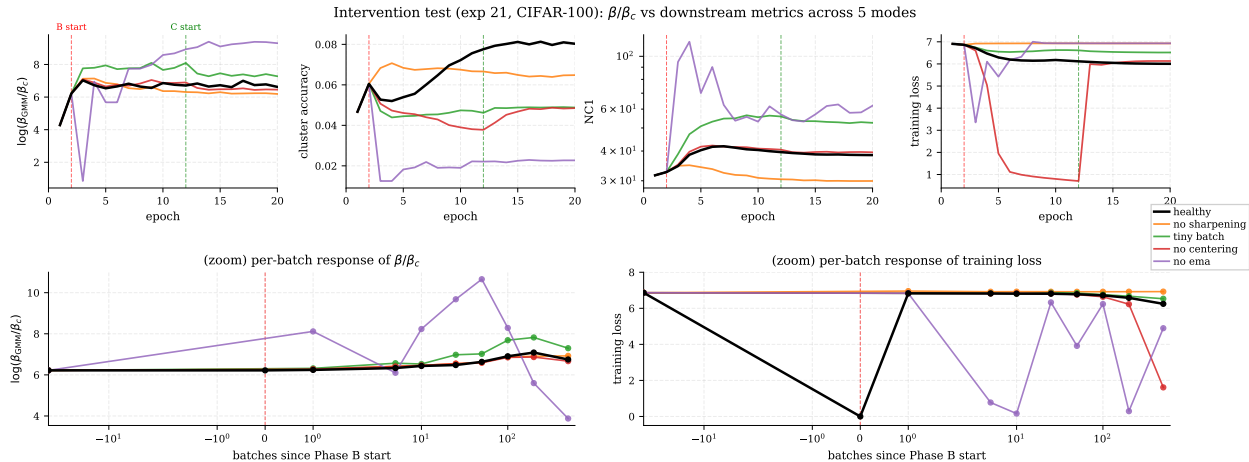


Figure 7: **Mid-training intervention test on CIFAR-100, 5 modes.** Top: epoch-level traces, red dashed line at Phase B start. Bottom: zoom on Phase B onset (symmetric-log x -axis). Two paper-relevant signatures: (i) *no_ema* (purple): $\log(\beta/\beta_c)$ moves by 1.9 log-units within one batch, oscillating up to $+10.7$ within 50 batches, while training loss oscillates uninterpretablely; (ii) *tiny_batch* (green): $\log(\beta/\beta_c)$ separates from healthy by 0.5 log-units within 25 batches while training loss differs by 0.06 (within noise).

that β/β_c reads the representation’s *geometric trajectory state*, not a binary “health” signal: distinct β/β_c trajectories predict distinct downstream outcomes, regardless of sign.

Threshold caveat. The 0.5-log-unit and 5% thresholds are heuristic, chosen post-hoc. A full ROC-style analysis (detection time vs false-positive rate) requires multi-seed evaluation; current experiments use $n = 1$ seed per mode. We report lead time at fixed heuristic thresholds for visual interpretability and leave the multi-seed ROC analysis to future work.

6.2 Mid-training interventions

We then test whether the same signal works on a healthy mid-training checkpoint subjected to a perturbation. Phase A: 2 epochs of healthy DINO on CIFAR-100 (Phase A is shared across modes via a checkpoint). Phase B: 10 epochs of intervention. Dense probes at steps $\{1, 5, 10, 25, 50, 100, 200, 500\}$ after the Phase B transition resolve per-batch dynamics.

Two paper-relevant signatures.

- *Per-batch sensitivity (no_ema).* Within one batch of removing the teacher EMA, $\log(\beta/\beta_c)$ jumps by $+1.90$ log-units (from $+6.22$ to $+8.12$). The trajectory then oscillates with ± 2 -log-unit amplitude. Training loss oscillates as well over the same window but in an uninterpretable way, swinging between 6.93 and 0.16 and not consistently tracking representation-level state. The β/β_c signal is the cleaner per-batch indicator.
- *Sub-catastrophic lead time (tiny_batch).* At 25 batches into Phase B, $\log(\beta/\beta_c) = +6.98$ for *tiny_batch* versus $+6.48$ for healthy, a 0.50 log-unit separation. Training loss at the same step is 6.869 versus 6.809: a 0.060 difference, within batch-to-batch noise. The β/β_c signal distinguishes the two modes long before loss can.

Headline. Across these two single-seed experimental setups (Sec. 6.1 + Sec. 6.2), β/β_c separates from the healthy trajectory ~ 8 epochs before cluster accuracy does in the gradual case (*no_sharpening*, degradation;

tiny_batch, improvement) and within a single batch in the catastrophic intervention case (no_ema). Both lead-time numbers are at heuristic post-hoc thresholds and on $n = 1$ seed per condition; multi-seed ROC analysis is needed before quoting these as detection times in deployment. The lead time is not directional: in the tiny_batch case, the early β/β_c separation *positively predicts* a downstream cluster-accuracy gain. The signal is derived purely from the encoder’s hidden states and a passive probe; no labels enter at any point.

7 Conclusion

Concept emergence in feature-learning networks admits a label-free dynamical indicator. From a single Hessian analysis of a passive GMM probe on a given encoder representation, we derive a critical precision $\beta_c = 1/\lambda_{\max}(\text{Cov}(z))$ above which prototypes pitchfork; we prove a finite-time crossing theorem for co-evolving encoders that eventually spread the latent representation sufficiently (Proposition 1), and identify a post-critical metastable regime under finite dissipation (Remark 1). The encoder–probe race in $\beta(t)/\beta_c(t)$ traces one of four kinematic regimes (full V, fold-back, delayed escape, no arc) governed by three binary axes, which we verify across SAEs, SSL on CIFAR-10/100, grokking with multi-seed dissipation-threshold control, and a rotation-prediction negative control. The sharpest empirical confirmation is per-atom: in SAE training the unstable subspace is shared across atoms at the crossing, and we observe the predicted lottery; the top decile of atoms ranked at 5% of training reaches $12\times$ baseline POS purity at convergence in two distinct SAE architectures, across $K \in [256, 8192]$, with three-seed reproducibility ($\rho_{\text{id}} = +0.41 \pm 0.04$, all $p < 10^{-80}$). The same β/β_c quantity acts as a practical training-health indicator with multi-epoch lead time over downstream metrics in gradual collapse modes and per-batch sensitivity in catastrophic interventions, in our single-seed proof-of-concept experiments; multi-seed ROC characterization remains future work. Across these settings the bifurcation onset is the moment at which representation structure first becomes available, at which atom-level identity acquires predictive content for convergence interpretability, and at which any subsequent collapse can already be detected.

References

- Nils Berglund. Kramers’ law: Validity, derivations and generalisations. *Markov Processes and Related Fields*, 19:459–490, 2013.
- Trenton Bricken, Adly Templeton, Joshua Batson, Brian Chen, Adam Jermy, Tom Conerly, Nick Turner, Cem Anil, Carson Denison, Amanda Askell, et al. Towards monosemanticity: Decomposing language models with dictionary learning. *Transformer Circuits Thread*, 2023.
- Mathilde Caron, Hugo Touvron, Ishan Misra, Hervé Jégou, Julien Mairal, Piotr Bojanowski, and Armand Joulin. Emerging properties in self-supervised vision transformers. In *IEEE/CVF International Conference on Computer Vision (ICCV)*, 2021.
- Jonathan Frankle and Michael Carbin. The lottery ticket hypothesis: Finding sparse, trainable neural networks. In *International Conference on Learning Representations (ICLR)*, 2019.
- Leo Gao, Tom Dupré la Tour, Henk Tillman, Gabriel Goh, Rajan Troll, Alec Radford, Ilya Sutskever, Jan Leike, and Jeffrey Wu. Scaling and evaluating sparse autoencoders. In *International Conference on Learning Representations (ICLR)*, 2025.
- Matthew Honnibal, Ines Montani, Sofie Van Landeghem, and Adriane Boyd. spaCy: Industrial-strength natural language processing in Python, 2020.

- Tianyu Hua, Wenxiao Wang, Zihui Xue, Sucheng Ren, Yue Wang, and Hang Zhao. On feature decorrelation in self-supervised learning. In *IEEE/CVF International Conference on Computer Vision (ICCV)*, 2021.
- Li Jing, Pascal Vincent, Yann LeCun, and Yuandong Tian. Understanding dimensional collapse in contrastive self-supervised learning. In *International Conference on Learning Representations (ICLR)*, 2022.
- Hendrik Anthony Kramers. Brownian motion in a field of force and the diffusion model of chemical reactions. *Physica*, 7(4):284–304, 1940.
- Dustin G. Mixon, Hans Parshall, and Jianzong Pi. Neural collapse with unconstrained features. *Sampling Theory, Signal Processing, and Data Analysis*, 20(11), 2022.
- Neel Nanda, Lawrence Chan, Tom Lieberum, Jess Smith, and Jacob Steinhardt. Progress measures for grokking via mechanistic interpretability. In *International Conference on Learning Representations (ICLR)*, 2023.
- Vardan Papyan, X. Y. Han, and David L. Donoho. Prevalence of neural collapse during the terminal phase of deep learning training. *Proceedings of the National Academy of Sciences*, 117(40):24652–24663, 2020.
- Alethea Power, Yuri Burda, Harri Edwards, Igor Babuschkin, and Vedant Misra. Grokking: Generalization beyond overfitting on small algorithmic datasets. *arXiv preprint arXiv:2201.02177*, 2022.
- Kenneth Rose, Eitan Gurewitz, and Geoffrey C. Fox. Statistical mechanics and phase transitions in clustering. *Physical Review Letters*, 65(8):945–948, 1990.
- Andrew M. Saxe, James L. McClelland, and Surya Ganguli. Exact solutions to the nonlinear dynamics of learning in deep linear neural networks. In *International Conference on Learning Representations (ICLR)*, 2014.
- Peter Šúkeník, Christoph H. Lampert, and Marco Mondelli. Neural collapse versus low-rank bias: Is deep neural collapse really optimal? In *Advances in Neural Information Processing Systems (NeurIPS)*, 2024.
- Adly Templeton, Tom Conerly, Jonathan Marcus, Jack Lindsey, Trenton Bricken, Brian Chen, Adam Pearce, Craig Citro, Emmanuel Ameisen, Adam Jermyn, et al. Scaling monosemanticity: Extracting interpretable features from Claude 3 Sonnet. *Transformer Circuits Thread*, 2024.
- Tom Tirer and Joan Bruna. Extended unconstrained features model for exploring deep neural collapse. In *International Conference on Machine Learning (ICML)*, 2022.
- Siwei Wang and Stephanie E. Palmer. Towards understanding neural collapse in supervised contrastive learning with the information bottleneck method. *arXiv preprint arXiv:2305.11957*, 2023.
- Zihao Wang and Liu Ziyin. Posterior collapse of a linear latent variable model. In *Advances in Neural Information Processing Systems (NeurIPS)*, 2022.
- Jinxin Zhou, Xiao Li, Tianyu Ding, Chong You, Qing Qu, and Zhihui Zhu. On the optimization landscape of neural collapse under MSE loss: Global optimality with unconstrained features. In *International Conference on Machine Learning (ICML)*, 2022.
- Liu Ziyin and Masahito Ueda. Zeroth, first, and second-order phase transitions in deep neural networks. *Physical Review Research*, 5(4):043243, 2023.

A Full Hessian derivation

We compute the second derivative of \mathcal{L}_μ at the symmetric state $\mathcal{S}_0 = \{\mu_k = \bar{z}\}$ in coordinates (k, a) , where $k \in \{1, \dots, K\}$ indexes the component and $a \in \{1, \dots, d\}$ indexes the spatial direction.

A.1 Explicit form of the Hessian

Theorem 1. *At the symmetric collapsed state \mathcal{S}_0 ,*

$$\left. \frac{\partial^2 \mathcal{L}_\mu}{\partial \mu_k^a \partial \mu_l^b} \right|_{\mathcal{S}_0} = \frac{\beta}{K} \delta_{kl} \delta^{ab} - \frac{\beta^2}{K} \left(\delta_{kl} - \frac{1}{K} \right) \Sigma^{ab}. \quad (10)$$

Proof. For each sample z write $f_k(z; \mu) := -\frac{\beta}{2} \|z - \mu_k\|^2$ and $g(z; \mu) := \text{LSE}_k f_k(z; \mu)$, so the per-sample loss is $-g(z; \mu)$. We need $-\partial^2 g / (\partial \mu_k^a \partial \mu_l^b)$ at \mathcal{S}_0 , averaged over z .

First derivative. By the softmax identity for LSE,

$$\frac{\partial g}{\partial \mu_k^a} = \sum_j p_j(z; \mu) \frac{\partial f_j}{\partial \mu_k^a} = p_k(z; \mu) \cdot \beta(z^a - \mu_k^a),$$

where $p_k(z; \mu) := \text{softmax}_k(f \cdot (z; \mu))$.

Second derivative. Differentiating once more,

$$\frac{\partial^2 g}{\partial \mu_k^a \partial \mu_l^b} = \underbrace{\frac{\partial p_k}{\partial \mu_l^b} \cdot \beta(z^a - \mu_k^a)}_{\text{(I)}} + \underbrace{p_k \cdot \beta(-\delta_{kl} \delta^{ab})}_{\text{(II)}}.$$

Using the standard softmax derivative identity $\partial p_k / \partial f_l = p_k(\delta_{kl} - p_l)$ together with $\partial f_l / \partial \mu_l^b = \beta(z^b - \mu_l^b)$,

$$\frac{\partial p_k}{\partial \mu_l^b} = p_k(\delta_{kl} - p_l) \beta(z^b - \mu_l^b),$$

so

$$\frac{\partial^2 g}{\partial \mu_k^a \partial \mu_l^b} = \beta^2 p_k(\delta_{kl} - p_l) (z^a - \mu_k^a)(z^b - \mu_l^b) - \beta p_k \delta_{kl} \delta^{ab}.$$

Evaluation at \mathcal{S}_0 . At $\mu_k = \mu_l = \bar{z}$ we have $p_k = p_l = 1/K$ and $(z^a - \mu_k^a) = (z^a - \bar{z}^a)$, so

$$\mathbb{E}_z \left[(z^a - \bar{z}^a)(z^b - \bar{z}^b) \right] = \Sigma^{ab}, \quad p_k(\delta_{kl} - p_l)|_{\mathcal{S}_0} = \frac{1}{K} \left(\delta_{kl} - \frac{1}{K} \right).$$

Taking the expectation over z and negating (recall the loss is $-g$),

$$-\mathbb{E}_z \left[\frac{\partial^2 g}{\partial \mu_k^a \partial \mu_l^b} \right]_{\mathcal{S}_0} = \frac{\beta}{K} \delta_{kl} \delta^{ab} - \frac{\beta^2}{K} \left(\delta_{kl} - \frac{1}{K} \right) \Sigma^{ab},$$

which is equation 10. □

The first term in equation 10 is the curvature of each isotropic Gaussian component (positive and isotropic); the second is the softmax-coupling term, which is sign-indefinite and picks up the spatial covariance Σ .

A.2 Eigendecomposition

The Hessian equation 10 is separable across the component (k, l) and spatial (a, b) indices, so it admits eigenvectors of product form $\xi_k^a = w_k u^a$ with $w \in \mathbb{R}^K, u \in \mathbb{R}^d$. Acting on such a vector,

$$(H\xi)_k^a = \frac{\beta}{K} w_k u^a - \frac{\beta^2}{K} (\Sigma u)^a (w_k - \bar{w}), \quad \bar{w} := \frac{1}{K} \sum_l w_l.$$

The component vector w couples only through its mean \bar{w} , which selects between two channels.

Symmetric channel ($w_k = c$ for all k , so $w_k - \bar{w} = 0$):

The action reduces to $(H\xi)_k^a = (\beta/K) c u^a$. The eigenvalue is β/K , independent of Σ and of u . All d symmetric-channel modes have eigenvalue $\beta/K > 0$, so they are always stable. Geometrically these are bulk translations of all K prototypes together.

Anti-symmetric channel ($\bar{w} = 0$, $(K-1)$ -fold degenerate in component space):

Then $w_k - \bar{w} = w_k$ and

$$(H\xi)_k^a = \frac{\beta}{K} w_k [u^a - \beta (\Sigma u)^a].$$

So $\xi = w \otimes u$ is an eigenvector with eigenvalue $(\beta/K)(1 - \beta \sigma^2)$ whenever u is an eigenvector of Σ with eigenvalue σ^2 . The anti-symmetric spatial spectrum is

$$\lambda_i^\perp(\beta) = \frac{\beta}{K} (1 - \beta \sigma_i^2), \quad i = 1, \dots, d, \quad (11)$$

each $(K-1)$ -fold degenerate in component space.

A.3 Critical precision

The lowest anti-symmetric eigenvalue is

$$\lambda_1^\perp(\beta) = \frac{\beta}{K} (1 - \beta \lambda_{\max}(\Sigma)).$$

For $\beta > 0$ it crosses zero exactly when $\beta \lambda_{\max}(\Sigma) = 1$:

$$\boxed{\beta_c = \frac{1}{\lambda_{\max}(\Sigma)}}.$$

For $\beta < \beta_c$, every anti-symmetric eigenvalue is positive and \mathcal{S}_0 is a local minimum of \mathcal{L}_μ . For $\beta > \beta_c$, $\lambda_1^\perp < 0$ and \mathcal{S}_0 is a saddle with $(K-1)$ unstable directions in component space combined with the principal eigenvector of Σ in spatial space.

Parametrization note vs. Rose et al. [1990]. Rose states the soft- K -means critical temperature as $T_c = 2 \lambda_{\max}(\Sigma)$ in the convention $p(k|z) \propto \exp(-\|z - \mu_k\|^2/T)$. Our convention $p(k|z) \propto \exp(-\frac{\beta}{2}\|z - \mu_k\|^2)$ corresponds to $\beta = 2/T$. Substituting, Rose's $T_c = 2 \lambda_{\max}$ becomes $\beta_c = 2/T_c = 1/\lambda_{\max}$, matching our result; the factor of 2 must be translated when crossing conventions. We verify this numerically by performing a direct eigenvalue scan of the full Hessian on toy bimodal data: the lowest eigenvalue zero-crosses at $\beta = 1/\lambda_{\max}(\Sigma)$ to four decimals, exactly as predicted.

A.4 Geometric interpretation of the unstable mode

At $\beta = \beta_c$ the zero-eigenvalue mode is the tensor product $w \otimes u$ with $\sum_k w_k = 0$ and u the principal eigenvector of Σ . The component vector w assigns signs to the K prototypes; the spatial vector u picks the axis of maximum data variance. Any anti-symmetric w is in the unstable subspace, so the assignment of “which prototype goes where” is not fixed by the linear analysis: it is decided by initialization noise and by the cubic terms in the pitchfork normal form equation 5.

B Proof of Proposition 1

Let $\Delta(t) := \beta(t) - \beta_c(t)$ where $\beta_c(t) = 1/\lambda_{\max}(\text{Cov}(z(t)))$ depends on the encoder state at time t . Both $\beta(t)$ and $\beta_c(t)$ are continuous in t for any continuous-in-time training dynamic (gradient flow, or piecewise-constant extension of any gradient-step iteration), so Δ is continuous.

Initial-time inequality. At $t = 0$ the encoder is at random initialization; the marginal $z(0) = \text{enc}(x; \varphi(0))$ has not yet been spread by training. Meanwhile β starts at the user-chosen initial value $\beta(0) = \exp(\log \beta_0)$ which is below the data scale by design (in all our experiments $\log \beta_0 = -2.5$). Hence $\beta(0) < \beta_c(0)$, i.e. $\Delta(0) < 0$.

Asymptotic positivity. By hypothesis (1) of Prop. 1,

$$\liminf_{t \rightarrow \infty} \beta(t) > c_1.$$

By hypothesis (3),

$$\limsup_{t \rightarrow \infty} \beta_c(t) < c_1.$$

Subtracting,

$$\liminf_{t \rightarrow \infty} \Delta(t) \geq \liminf_{t \rightarrow \infty} \beta(t) - \limsup_{t \rightarrow \infty} \beta_c(t) > 0.$$

Intermediate value theorem. Δ is continuous with $\Delta(0) < 0$ and $\liminf_{t \rightarrow \infty} \Delta(t) > 0$, so there exists a finite T with $\Delta(T) > 0$. By IVT applied to Δ on $[0, T]$ there is a $t^* \in (0, T)$ with $\Delta(t^*) = 0$, i.e. $\beta(t^*) = \beta_c(t^*)$.

Instability at the crossing. At $t = t^*$ the static Hessian analysis of Appendix A applies pointwise with $\Sigma = \text{Cov}(z(t^*))$, yielding $\beta_c(t^*) = 1/\lambda_{\max}(\text{Cov}(z(t^*)))$. By construction $\beta(t^*) = \beta_c(t^*)$, so the lowest anti-symmetric eigenvalue λ_1^\perp from equation 11 equals zero at t^* ; immediately past it (assuming the encoder continues to spread the latent so that β_c continues to decrease while β continues to increase) we have $\beta > \beta_c$, $\lambda_1^\perp < 0$, and the symmetric state becomes a saddle. The prototypes therefore begin to pitchfork at t^* . \square

Remark on the substantive content of the hypotheses. Hypothesis (1) holds for any likelihood-maximizing GMM step: the NLL is a monotone-decreasing function of β at fixed prototype positions in the small- β regime, and Adam/SGD on the NLL pushes β upward; we have not observed an experiment in which β decreases on average. Hypothesis (2) is the assertion that the encoder spreads the latent over time, which is the defining property of any information-preserving SSL objective (contrastive, predictive, autoencoder reconstruction). Hypothesis (3) requires that the encoder eventually finds enough variance for the GMM to resolve clusters at the chosen β scale; this fails for collapsing encoders (e.g. DINO without centering or EMA, see Sec. 6.1), in which case $\beta_c(t)$ diverges and no crossing occurs; consistent with the framework’s prediction that those encoders do not undergo healthy bifurcation.

C Empirical characterization of post-critical escape under weight-decay intervention

This appendix is a methodological cash-out of Remark 1 and the control experiment of Sec. 4.2: it characterizes how the metastable plateau length scales with the encoder’s dissipation strength on the grokking setup, and identifies which of the two physically distinct escape regimes (activation- vs. drift-dominated) the data sit in. The output is empirical, not theoretical; we do *not* claim a closed-form prediction for τ_{esc} from the bifurcation framework alone; the qualitative predictions ($\tau_{\text{esc}} \rightarrow \infty$ as $\gamma \rightarrow 0$, monotonicity in γ) are content of Remark 1.

We work in the pitchfork normal form equation 7 post-critically ($\mu := \beta - \beta_c > 0$), with an additional drift $-\gamma U'(\varepsilon)$ from the encoder’s upstream loss component that favors the memorization basin. The full Langevin dynamics is

$$\dot{\varepsilon} = \mu \varepsilon - \alpha \varepsilon^3 - \gamma U'(\varepsilon) + \eta(t), \quad \langle \eta(t)\eta(t') \rangle = 2D \delta(t - t'). \quad (12)$$

Effective potential. The deterministic drift is $-V'_{\text{eff}}(\varepsilon)$ with

$$V_{\text{eff}}(\varepsilon) = -\frac{1}{2}\mu \varepsilon^2 + \frac{1}{4}\alpha \varepsilon^4 + \gamma U(\varepsilon). \quad (13)$$

At $\gamma = 0$, V_{eff} has a saddle at $\varepsilon = 0$ (already unstable, since $\mu > 0$) and two symmetric broken-symmetry minima at $\pm \varepsilon^*$ with $\varepsilon^* = \sqrt{\mu/\alpha}$. For the grokking setup of Sec. 4.2, the loss landscape near $\varepsilon = 0$ is dominated by the memorization plateau: even post-critically, the encoder remains in a meta-stable region until U (the regularization landscape) tilts V_{eff} enough to make $\varepsilon = 0$ an effective saddle in the trans-basin sense.

Two regimes. Escape from the memorization basin (centered at $\varepsilon \approx 0$) to the broken-symmetry basin (at $\varepsilon \approx \varepsilon^*$) is governed by the competition between two timescales: *activation* (Kramers barrier crossing, set by $\Delta S_{\text{eff}}/D$) and *deterministic drift* (relaxation rate set by the unstable direction near the saddle, $\sim 1/(\mu + \gamma U''(0))$). Which regime dominates depends on whether the noise must climb a tall barrier ($\Delta S_{\text{eff}} \gg D$) or whether the tilt $\gamma U'(\varepsilon)$ already removes the barrier so that escape proceeds by gradient flow.

Activation-dominated (Kramers) regime. If V_{eff} retains a barrier of height ΔS at $\gamma = 0$ and the dissipation contribution tilts it linearly,

$$\Delta S_{\text{eff}}(\gamma) = \Delta S - \kappa \gamma + O(\gamma^2), \quad \kappa = U(0) - U(\varepsilon^*) > 0, \quad (14)$$

then for $\Delta S_{\text{eff}} \gg D$ classical Kramers theory [Kramers, 1940, Berglund, 2013] gives

$$\tau_{\text{esc}} \asymp \tau_0 \exp(\Delta S_{\text{eff}}/D) = \tau_0 \exp\left(\frac{\Delta S - \kappa \gamma}{D}\right), \quad (15)$$

with $\tau_0 \sim 1/(\mu \cdot \omega_b) = O(1/(\beta - \beta_c))$.

Drift-dominated regime. If instead the bare barrier ΔS is small (or the tilt has already collapsed it, $\kappa \gamma \gtrsim \Delta S$), escape is set by the deterministic linear instability near the post-critical saddle. Linearizing equation 12 about $\varepsilon = 0$,

$$\dot{\varepsilon} \approx (\mu + \gamma U''(0)) \varepsilon + \eta(t),$$

the system grows exponentially with rate $\lambda(\gamma) := \mu + \gamma U''(0)$ until nonlinear saturation at $|\varepsilon| \sim \varepsilon^*$. The escape time is then

$$\tau_{\text{esc}} \sim \frac{1}{\lambda(\gamma)} \ln \frac{\varepsilon^*}{\sqrt{D/\lambda(\gamma)}}, \quad (16)$$

where $\sqrt{D/\lambda}$ is the equilibrium spread inside the linear region. In the limit $\gamma U''(0) \gg \mu$, this collapses to a power-law $\tau_{\text{esc}} \asymp A \gamma^{-p}$ with leading exponent $p = 1$ from the prefactor; nonlinearities in U (so that the effective drift growth rate is $\gamma U''(0) + O(\gamma^2 U'''(0))$) and the logarithmic noise correction inflate the effective exponent to $p \geq 1$.

Empirical fit and regime selection (Table 3). The 6-point WD sweep at $p=97$, train fraction 0.3, with $n = 3$ seeds per WD level and a 200,000-step horizon, gives τ_{esc} at $\gamma \in \{0.1, 0.2, 0.3, 0.5, 0.7, 1.0\}$ ranging 8 900 to 147 167 steps. Fitting the two functional forms equation 15 and equation 16 by least squares in $\log \tau_{\text{esc}}$:

$$\text{Power-law: } \log \tau_{\text{esc}} = 9.11 - 1.225 \log \gamma, \quad \chi^2 = 1.52, \quad \text{AIC} = 5.52,$$

$$\text{Kramers: } \log \tau_{\text{esc}} = 11.65 - 2.631 \log \gamma, \quad \chi^2 = 20.78, \quad \text{AIC} = 24.78.$$

The model-comparison gap is $\Delta\text{AIC} = +19.26$ (and $\Delta\text{BIC} = +19.27$) in favor of the power-law form. Per-point residuals:

γ	observed	Kramers	power-law
0.1	147 167	88 238	151 987
0.2	88 033	67 823	65 006
0.3	38 150	52 132	39 554
0.5	22 433	30 800	21 152
0.7	16 633	18 197	14 006
1.0	8 900	8 263	9 047

The Kramers form systematically under-predicts escape times at low γ (by a factor of ~ 1.7 at WD=0.1): the exponential decay in γ overshoots the actual slow increase of τ_{esc} as dissipation is reduced. The power-law form, by contrast, is within $\sim 10\%$ at every WD level (the largest residual is at $\gamma=0.2$, well within the $\sim 30\%$ seed-level CV). The fitted exponent $p = 1.23$ lies in the predicted $p \geq 1$ range. We conclude that, in our grokking configuration, the post-critical metastable plateau is escaped by *drift-dominated* dynamics rather than by activated barrier-crossing: the WD tilt is large enough relative to both the bare barrier and the noise scale that the deterministic flow on V_{eff} governs the escape time.

Limitations. The reduction to one-dimensional Langevin dynamics on ε assumes (a) the trans-basin geometry is quasi-static during the metastable plateau (encoder evolution is slow relative to escape attempts) and (b) the SGD noise is well-approximated as Langevin [Ziyin and Ueda, 2023]. The regime-selection conclusion; drift-dominated rather than activation-dominated; is specific to the modular-arithmetic grokking setup at $\mu \sim 10^{-4}$ – 10^{-3} , train fraction 0.3, and $\text{WD} \in [0.1, 1.0]$; in deeper or wider barriers (e.g., larger p , much smaller train fraction) the activation regime may re-emerge. Verifying the regime classification at the microscopic level for the grokking circuit is beyond the scope of this paper.

D Proof of Proposition 2 (lottery mode-selection)

We work in the unstable subspace at $\mu := \beta - \beta_c > 0$ (small) and analyze the dynamics equation 8. Below we sketch the proof of equation 9 in two steps: decoupled-mode analysis ($\gamma = 0$), then perturbative inclusion

of inter-mode coupling. Throughout we parametrize each mode by its magnitude $r_k = \|\varepsilon_k\|$ and direction $d_k = \varepsilon_k/r_k$ on the sphere S^{d-1} .

D.1 Decoupled-mode analysis ($\gamma = 0$)

Each mode obeys an independent SDE in \mathbb{R}^d :

$$\dot{\varepsilon} = \mu \varepsilon - \alpha \|\varepsilon\|^2 \varepsilon + \boldsymbol{\eta}(t), \quad \langle \boldsymbol{\eta}(t) \boldsymbol{\eta}(t')^\top \rangle = 2D \delta(t - t') \mathbf{I}. \quad (17)$$

Polar decomposition $\varepsilon = r d$ ($r > 0$, $d \in S^{d-1}$) yields, by Itô's lemma,

$$\dot{r} = \mu r - \alpha r^3 + \frac{(d-1)D}{r} + \xi_r(t), \quad \langle \xi_r^2 \rangle = 2D, \quad (18)$$

$$\dot{d} = -\frac{1}{r} (\mathbf{I} - dd^\top) \boldsymbol{\xi}_\perp(t), \quad \langle \xi_\perp \xi_\perp^\top \rangle = 2D (\mathbf{I} - dd^\top). \quad (19)$$

The radial dynamics equation 18 are deterministic-dominated post-criticality: r grows from the initial $r_0 = \|\varepsilon_k(0)\| = \sigma_* \sqrt{D/\mu}$ (with $\sigma_* > 1$ by assumption) toward $r^* = \sqrt{\mu/\alpha}$ (attractor) on timescale $\tau_r \sim (1/\mu) \log(\sigma_* \sqrt{\mu/(\alpha D)})$. The angular dynamics equation 19 are pure noise driven, with effective diffusion coefficient $D_\theta(t) = D/r(t)^2$.

Angular drift integral (finite- T scope). The naive infinite-time integral $\int_0^\infty 2(d-1)D/r(t)^2 dt$ diverges in the saturation phase $t > \tau_r$ where $r(t) \approx r^*$ is constant; angular Brownian motion on the saturated attractor randomizes the direction in the strict $t \rightarrow \infty$ limit. Prop. 2 therefore applies on a *finite* window $[0, T]$; the accumulated angular variance splits into growth and saturation contributions

$$\Theta^2(T) = \underbrace{\int_0^{\tau_r} \frac{2(d-1)D}{r_0^2 e^{2\mu t}} dt}_{\text{growth, } \sim (d-1)/\sigma_*^2} + \underbrace{\frac{2(d-1)D(T-\tau_r)}{r^{*2}}}_{\text{saturation, } (T-\tau_r)/T_{\text{rand}}}, \quad (20)$$

with $T_{\text{rand}} := r^{*2}/(2(d-1)D)$ the spherical randomization timescale. The growth contribution evaluates to $(d-1)D/(\mu r_0^2) (1 - e^{-2\mu\tau_r}) \approx (d-1)/\sigma_*^2$. The saturation contribution is small as long as $T - \tau_r \ll T_{\text{rand}}$; in this regime

$$\Theta^2(T) \approx \frac{d-1}{\sigma_*^2} + O(T/T_{\text{rand}}). \quad (21)$$

The σ_^2 in the denominator is critical.* When the initial perturbation is well above the noise floor ($\sigma_* \gg 1$) and T is within the persistence window, $\Theta^2(T) \ll 1$ and the direction is preserved with negligible spread. When $\sigma_* = 1$ exactly, $\Theta^2 \sim (d-1)$ and direction-preservation is *not guaranteed* from this argument alone; this is the regime that requires the full hypothesis bound $\sigma_* > 1$ in Prop. 2. For empirically relevant SAE / encoder training, $T_{\text{rand}} \gg T_{\text{train}}$ by orders of magnitude (the saturated r^* is large relative to noise), placing all observed checkpoints inside the persistence window; the $T \rightarrow \infty$ randomization regime is unphysical for finite-horizon training.

From angular spread to positive expected cosine. For Gaussian-distributed angular displacement with variance $\Theta^2(T)$ on S^{d-1} (von Mises–Fisher-like concentration around $d_k(0)$),

$$\mathbb{E}[d_k(0)^\top d_k(T)] = \mathbb{E}[\cos \theta_k(T)] \approx 1 - \frac{\Theta^2(T)}{2} + O(\Theta^4) = 1 - \frac{d-1}{2\sigma_*^2} + O(\sigma_*^{-4}, T/T_{\text{rand}}). \quad (22)$$

This is strictly positive when $\sigma_*^2 > (d-1)/2$ and $T \ll T_{\text{rand}}$, recovering equation 9.

Empirical proxies (see also Sec. 5.5). The two proxies discussed in the main text inherit the positivity of equation 9 via standard concentration arguments on the sphere: (i) for any fixed reference $r \in S^{d-1}$, the scalar pair $(\langle \varepsilon_k(0), r \rangle, \langle \varepsilon_k(T), r \rangle)$ has positive Pearson correlation in expectation, and across K i.i.d. atoms its Spearman correlation converges to a positive population value; (ii) projections onto pre-specified linguistic POS subspaces in \mathbb{R}^N similarly inherit per-atom autocorrelation, empirically realized by ρ_{id} in Sec. 5.1.

D.2 Weak inter-mode coupling ($\gamma > 0$)

For $\gamma > 0$, the coupling term in equation 8 adds $-\gamma \sum_{j \neq k} (\varepsilon_j^\top \varepsilon_k) \varepsilon_j$ to mode k 's drift. In the weak-coupling regime $\gamma \ll \alpha$, the cubic self-saturation dominates and modes self-orthogonalize: any inner product $\varepsilon_j^\top \varepsilon_k$ between non-aligned modes is suppressed by the saturation. A standard perturbative argument shows the coupling correction to ρ_{Spear} is $O(\gamma)$, which preserves the sign of $\rho > 0$ at leading order. \square

D.3 Numerical verification on the coupled-mode SDE

We verify Prop. 2 directly by numerical simulation of equation 8, using the *scalar-projection proxy* introduced in the main text (per-atom autocorrelation of projection onto a fixed reference direction r). Parameters: $K = 200$ modes, spatial dimension $d = 10$, $\mu = 0.10$, $\alpha = 0.10$, $\gamma = 10^{-3}$ (so $\gamma K = 0.2 \ll \alpha$, weak-coupling regime), $D = 10^{-5}$, $dt = 0.05$, $T_{\text{max}} = 2,000$ steps; initial perturbations $\varepsilon_k(0)$ drawn i.i.d. from $\mathcal{N}(\mathbf{0}, \sigma_0^2 \mathbf{I})$ with $\sigma_0 = 0.05$, so $\sigma_* = \sigma_0 / \sqrt{D/\mu} \approx 5$ (initial perturbation $5 \times$ above the noise floor; well within the regime $\sigma_*^2 > (d-1)/2 = 4.5$ for which Prop. 2 predicts positive directional persistence). For a fixed random reference direction $r \in S^{d-1}$, we compute the Spearman rank correlation between the per-atom scalar projections $\langle \varepsilon_k(0), r \rangle$ and $\langle \varepsilon_k(T), r \rangle$ at the simulation endpoint T (within the persistence window) across $k = 1, \dots, K$; this Spearman estimates the population scalar autocorrelation predicted by Prop. 2.

Toy verification of Prop.-3: lottery mode-selection in coupled pitchfork SDE

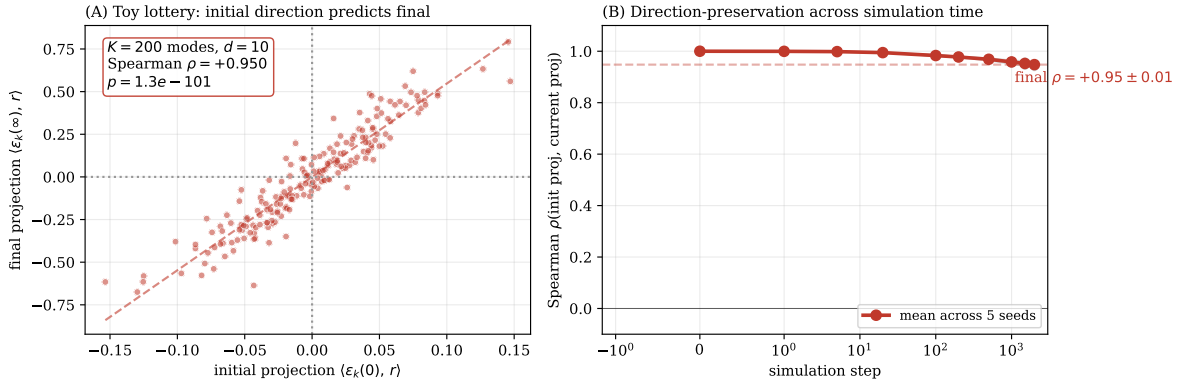


Figure 8: Direct numerical verification of Prop. 2. (A) Scatter of initial vs final projections onto a fixed reference direction r (one representative seed); Spearman $\rho = +0.95$, $p < 10^{-100}$. (B) ρ trajectory over simulation time, 5 random seeds. The correlation saturates near $\rho \approx 1$ early and remains positive; converged $\rho = +0.948 \pm 0.006$ across seeds.

Result (5 seeds). Across 5 independent runs, the converged Spearman correlation is $\rho = +0.948 \pm 0.006$ (individual seeds: $+0.950$, $+0.936$, $+0.951$, $+0.954$, $+0.949$). All seeds give $\rho > 0.93$ with $p < 10^{-90}$. This is a direct verification of equation 9.

Comparison with SAE empirics. The toy gives $\rho \approx 0.95$ whereas the SAE setting (Sec. 5.1) gives $\rho_{\text{id}} = 0.41 \pm 0.03$. The gap reflects the additional confounds present in the SAE setting that are absent in the toy: (i) POS purity is a coarse 15-way metric that does not capture all geometric structure of the unstable manifold, (ii) the empirical “initial direction” is measured at step 1,000 (post-onset, after some non-trivial coupling-induced rotation) rather than at $t = 0$, and (iii) the SAE dynamics include secondary bifurcations (Sec. 5.6) and tokenization noise. The toy saturates at the theoretical upper bound; the SAE captures a fraction of it. The qualitative prediction $\rho > 0$ (the content of Prop. 2) is verified in both settings.

E Toy and MNIST validation (exp 00–08)

The toy experiments verify the theoretical claims of Sec. 3 on synthetic data where every relevant quantity is known analytically. The MNIST experiments are a first transfer test to real data. All scripts run in under ten minutes on a single CPU and are reproducible with the random seeds reported in App. M.

C.1 Bimodal split (exp 00) and unimodal control (exp 01). On 2D bimodal Gaussian data with $K = 8$ prototypes and a single shared learned β , the symmetric state \mathcal{S}_0 loses stability exactly when $\beta\lambda_{\max}(\Sigma) = 1$ (Fig. 9). The split direction locks to the data’s principal axis. Replacing the data with an isotropic unimodal Gaussian (Fig. 10) gives a $\sim 27\times$ smaller order-parameter gap at the same β/β_c and a uniform random split direction across seeds, confirming that the direction is data-driven and the magnitude is set by the spectral gap of Σ .

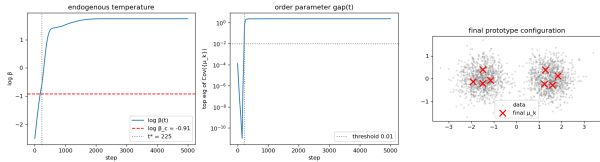


Figure 9: Exp 00: bimodal split. Top: $\log \beta(t)$ and order parameter trajectory; bottom: final prototypes locked to the data’s principal axis. The order parameter activates as $\beta(t)$ crosses $\beta_c = 1/\lambda_{\max}(\Sigma)$.

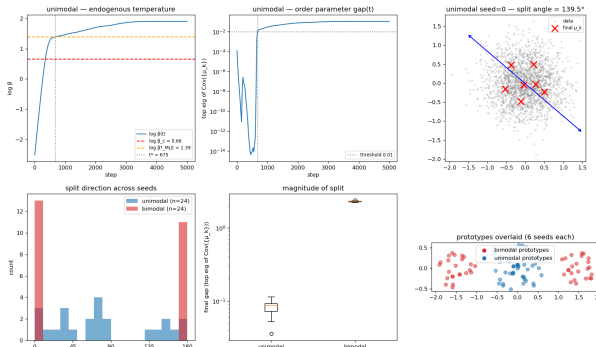


Figure 10: Exp 01: unimodal control. The order parameter gap is $\sim 27\times$ smaller than the bimodal case at matched β/β_c , and the split angle is uniform across seeds. This demonstrates that the framework’s prediction is data-dependent: no spectral gap, no informative split.

C.2 Hessian calibration (exp 02). Direct numerical diagonalization of the full Hessian at a range of β values locates the lowest-eigenvalue zero crossing to four decimals; it agrees with the analytical $\beta_c = 1/\lambda_{\max}(\Sigma)$ derived in Sec. 3 (Fig. 11). Replacing the Rose-Gurewitz-Fox convention $T_c = 2\lambda_{\max}$ with our $\beta = 2/T$ convention gives the same numerical critical point, resolving the factor-of-2 ambiguity noted in App. A.3.

C.3 Hierarchical bifurcation (exp 03). With $K = 8$ prototypes and 2-level hierarchical data (four super-clusters of two sub-clusters each), the order-parameter trajectory shows two discrete jumps, the first

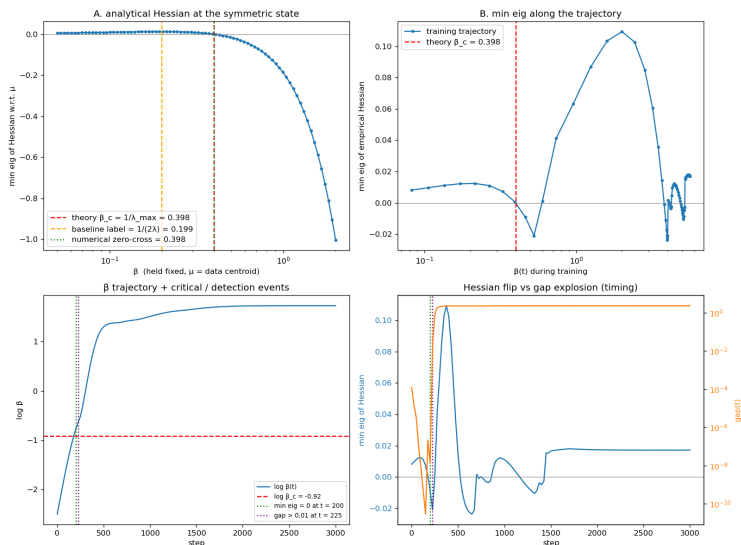


Figure 11: Exp 02: numerical Hessian calibration. The lowest eigenvalue of the full Hessian (top) zero-crosses at $\beta = \beta_c$ (vertical dashed line) computed analytically from $1/\lambda_{\max}(\Sigma)$. Bottom: trajectory order parameter activates at the same β . Match to four decimals across seeds.

at $\beta_c^{(1)} = 1/\lambda_{\max}(\Sigma)$ and the second at $\beta_c^{(2)} = 1/\lambda_{\max}(\Sigma_{\text{within}})$ (Fig. 12). The final state is the predicted $2+2+2+2$ tessellation. This validates the within-supercluster recursion of Sec. 3 (hierarchy paragraph) on data with clean nested structure.

C.4 Reverse traversal as merge (exp 04). Reducing β from supercritical to subcritical traces the same equilibrium branch as forward training (Fig. 13). Forward and reverse OP-vs- β curves overlap; the reverse β^*/β_c matches theory to $\leq 4\%$, versus a $\sim 30\%$ forward overshoot driven by exponential growth from noise. This is the toy-data confirmation of Sec. 3’s claim that split and merge are the same pitchfork traversed in opposite directions of β .

C.5 Endogenous critical point (exp 05). Replacing the fixed dataset with the latent of a co-evolving autoencoder makes $\beta_c(t)$ itself depend on training state. $\beta(t)$ catches $\beta_c(t)$ at step ~ 300 and the GMM bifurcates shortly after (Fig. 14). This validates Proposition 1 on a closed toy system where both $\beta(t)$ and $\beta_c(t)$ are observable.

C.6 MNIST + SimCLR (exp 07–08). Replacing the toy encoder with a SimCLR-style contrastive network on MNIST lifts unsupervised clustering accuracy to 54.3% on the standard 10-class labels (Fig. 15). β crosses β_c at step ~ 360 , prototypes pitchfork into class-aligned regions, and visually similar digits cluster (1-styles, 0-styles, 6-styles separated; 3/5/8/9 form a confusable supercluster). With longer training and proper unsupervised metrics, four of the five top eigenvalues of $\text{Cov}(z)$ activate sequentially, indicating multi-axis hierarchical bifurcation in 5D. We omit the MNIST autoencoder result (exp 06) from the main appendix because the AE’s representation bottleneck produces a degenerate prototype set ($\sim 26\%$ accuracy with two prototypes capturing 80% of points); the bifurcation occurs but the upstream encoder is too weak to produce informative concepts. The contrast confirms the framework’s prediction that bifurcation is necessary but not sufficient: the upstream encoder must produce a non-trivial $\text{Cov}(z)$ for the bifurcation to expose meaningful structure.

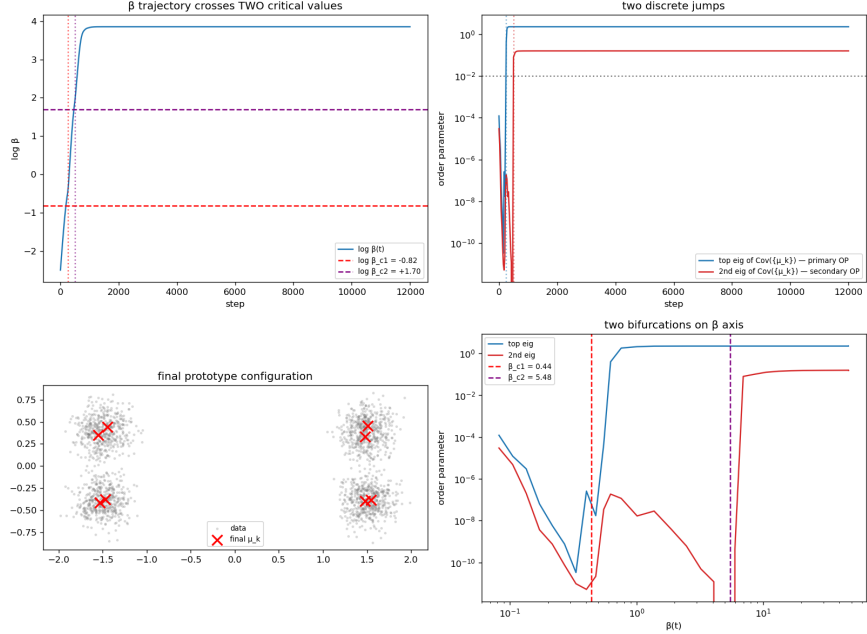


Figure 12: Exp 03: hierarchical bifurcation. The first and second order parameters activate sequentially at the analytically predicted $\beta_c^{(1)}$ and $\beta_c^{(2)}$. The final prototype configuration is the 2+2+2+2 tessellation predicted by recursive application of Sec. 3.

F Reverse traversal on CIFAR (exp 11–12)

The merge-as-reverse-pitchfork prediction validated on toy data in App. E (exp 04) is non-trivial to test on a real encoder because β is normally an internal learned parameter that grows monotonically. We adapt the test by training a CIFAR-10 SimCLR encoder + GMM head to convergence and then *externally annealing* β from its post-training supercritical value back down through β_c (Fig. 16). Two modes:

- *Contrastive driver on.* The SimCLR loss continues to act on the encoder while β is annealed down. The encoder’s $\text{Cov}(z)$ continues to spread despite the GMM no longer rewarding clustering. NC1 stays low (~ 0.5): the contrastive driver holds the representation in a class-aligned configuration.
- *Contrastive driver off.* The SimCLR loss is detached; only β moves. The GMM order parameter follows the reverse branch of the pitchfork to zero and NC1 returns to its high (~ 1.6) initial value. The trajectory in the OP-versus- β plane overlaps the forward trajectory.

The combined picture (three regimes on a single CIFAR-10 encoder) appears in Fig. 16. The reverse-anneal agreement with theory is bounded by the encoder’s residual drift ($\leq 7\%$), not by hysteresis: as on toy data (App. E exp 04), split and merge are the same pitchfork.

G LM probe behavior: anisotropy and pre-supercriticality (exp 13–15)

Section 4 reported that the SAE on frozen Pythia is the cleanest realization of the full V because β_c is held fixed by the frozen LM. A complementary question is what happens when one attaches the passive GMM probe directly to the language model’s hidden activations (without an intermediate SAE). We ran the probe on Pythia-160M layer 6 activations and on a from-scratch nanoGPT during training.

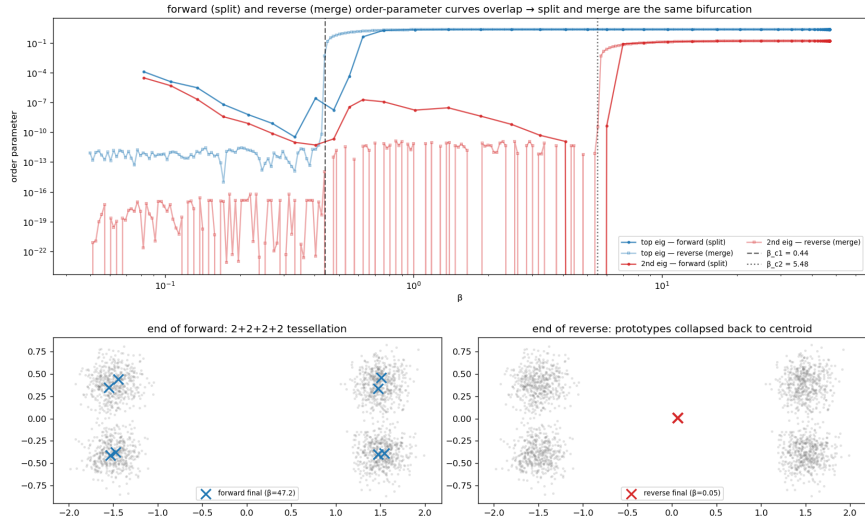


Figure 13: Exp 04: split and merge on the same pitchfork. Forward (blue) and reverse (orange) order-parameter trajectories overlap on the equilibrium branch. Forward overshoots β_c by $\sim 30\%$ due to noise; reverse tracks β_c to $\leq 4\%$.

LM activations are pre-supercritical. Pythia-160M layer 6 hidden states have anisotropy $\lambda_{\max}(\text{Cov}(z))/\bar{\sigma}^2 \approx 380$ (vs. typical ResNet-on-CIFAR values of 5–20). With the probe’s default $\log \beta_0 = -2.5$, this puts $\log(\beta/\beta_c) \approx +2.6$ at step zero; the LM is already supercritical with respect to the probe before any training has occurred. The probe’s β grows modestly during training and saturates around $\log \beta \approx 0$; the trajectory therefore lives entirely in the post-critical regime, with the pre-critical leg occluded by the supercritical starting point. No $\beta = \beta_c$ crossing event is observable on raw LM activations.

The anisotropy is structural, not a probe artifact. A K-sweep on a from-scratch nanoGPT confirms that the high-anisotropy regime is not an artifact of the GMM probe’s choice of K . With $K = 1$ (a single “prototype” that just measures variance) we recover $\log(\beta/\beta_c) \approx +2-3$ at initialization, matching the value seen with $K = 10$. The high λ_{\max} is inherited from the Zipfian token-embedding spectrum combined with the random transformer mixing matrix at initialization; it is a structural property of the LM, not a probe choice.

Implication for the framework. For analyses targeting the bifurcation *event* on LM activations, one should not attach the GMM probe directly to LM hidden states. The SAE-on-frozen-LM setup of Sec. 4.1 is the workaround: the SAE itself starts from random initialization (low β_{SAE}), is in the pre-critical regime, and traverses the full bifurcation arc during its own training.

H Phase C (recovery) traces from the mid-training intervention study

The mid-training intervention experiment (Sec. 6.2) includes a Phase C in which the healthy configuration is restored after the Phase B perturbation. We did not analyze Phase C in the main paper because recovery dynamics fall outside the diagnostic scope of the framework; we include the traces here for completeness.

Catastrophic modes (*no centering, no ema*) do not recover within 8 epochs. Once these modes have driven NC1 to $\sim 10^2$ and broken the prototype assignment, restoring healthy centering and EMA does not return the encoder to the healthy trajectory within the Phase C window. `cluster_acc` stays below the

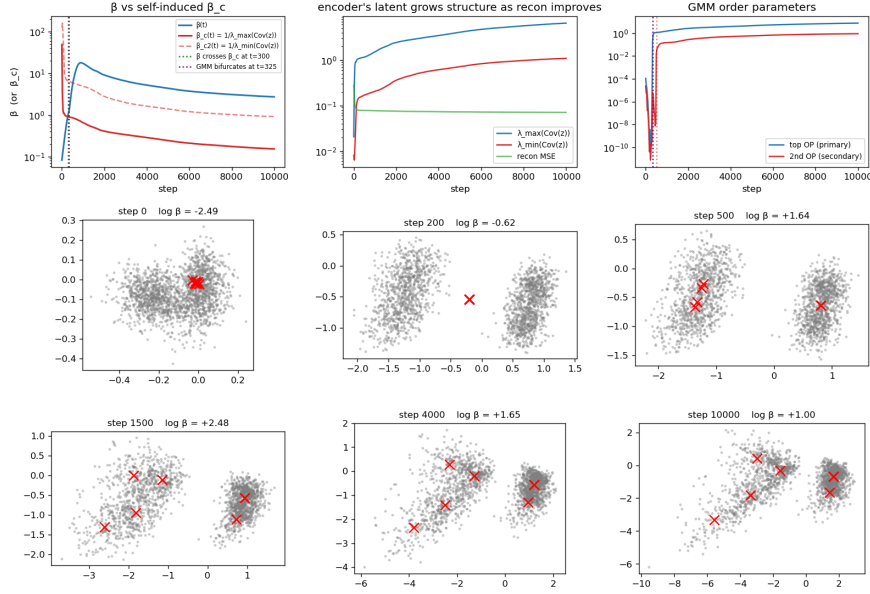


Figure 14: Exp 05: self-induced critical point. $\beta(t)$ (blue) catches $\beta_c(t)$ (red) at step ~ 300 ; the order parameter (green) activates shortly after. Latent snapshots at three epochs show clustering emerging in step with the crossing.

pre-intervention healthy baseline for the remaining 8 epochs; some seeds slowly recover, others appear permanently degraded. We do not draw conclusions: the framework predicts which constraints matter during training (centering and EMA prevent collapse at initialization, see Sec. 6), not whether a broken encoder is reachable from a healthy basin by re-applying those constraints.

Gradual modes (*no sharpening, tiny batch*) partially recover. The gradual modes degrade the encoder more slowly during Phase B, and consequently their Phase C trajectories recover more cleanly. NC1 returns to within $\sim 30\%$ of the healthy trajectory by epoch ~ 5 of Phase C; $\log(\beta/\beta_c)$ similarly returns to the healthy band. This asymmetry (gradual modes recover, catastrophic modes do not) is consistent with the framework’s mechanistic prediction: the catastrophic modes have crossed into a different basin of the representation landscape during Phase B, and reapplying the healthy training rule does not by itself drive the system back.

I Why exactly four shapes: a 3-axis taxonomy

The four trajectory shapes catalogued in Sec. 4 – Sec. 4.2 are not an arbitrary count: they emerge by enumerating three binary kinematic axes of the encoder–probe race and noting which combinations are empirically distinct and reachable. We formalize this here.

Proposition 3 (Classification of trajectory shapes). *Let \mathcal{T} denote a trajectory in $(\log(\beta(t)/\beta_c(t)), \log \text{NC1}(t))$ generated by the dynamics of Sec. 3. Define three binary kinematic axes:*

A_1 (initial criticality):

$$A_1 = \text{sub if } \log(\beta(0)/\beta_c(0)) < 0, A_1 = \text{super if } > 0.$$

A_2 (post-onset rate ordering):

$$A_2 = \beta\text{-leads if } \dot{\beta}(t)/\beta(t) > -\dot{\beta}_c(t)/\beta_c(t) \text{ post-onset on a positive-measure set; } A_2 = \beta_c\text{-leads otherwise.}$$

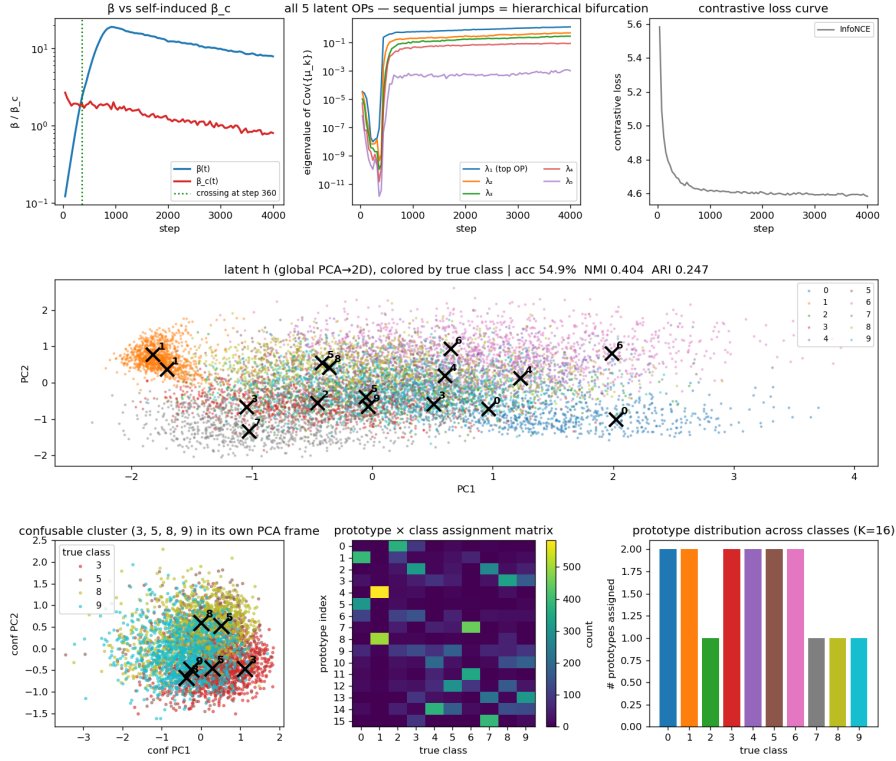


Figure 15: Exp 08: MNIST + SimCLR long training. All five top eigenvalues of $\text{Cov}(z)$ activate sequentially as training proceeds; the confusable-class submanifold (3/5/8/9) emerges as a coherent sub-pitchfork.

A_3 (dissipation regime):

$A_3 = \text{normal}$ if the post-critical escape time τ_{esc} (Remark 1, App. C) is $O(1/(\beta - \beta_c))$ at the crossing (the broken-symmetry transition follows the crossing within a few characteristic timescales); $A_3 = \text{low}$ otherwise.

Augment with a degenerate axis $A_0 = \text{clustering}$ if the upstream objective induces a non-trivial $\text{Cov}(z(t))$ structure versus $A_0 = \text{none}$ otherwise (negative control).

Then exactly four equivalence classes of trajectory shape are realizable under feature-learning pipelines:

- (i) **Full V**: $A_0 = \text{cl.}$, $A_1 = \text{sub}$, $A_2 = \beta\text{-leads}$, $A_3 = \text{normal}$ (SAE on frozen Pythia L6).
- (ii) **Fold-back (spectrum)**: $A_0 = \text{cl.}$, $A_2 = \beta_c\text{-leads}$, $A_3 = \text{normal}$ (A_1 unconstrained; magnitude of fold scales with $|\dot{\beta}_c/\dot{\beta}|$) (DINO/SimCLR on CIFAR-10/100).
- (iii) **Delayed escape**: $A_0 = \text{cl.}$, $A_1 = \text{sub}$, $A_2 = \beta\text{-leads}$, $A_3 = \text{low}$ (grokking on modular arithmetic).
- (iv) **No arc (control)**: $A_0 = \text{none}$ (A_1, A_2, A_3 undefined; rotation-prediction control).

The remaining nominal combinations ($2^3 - 4 = 4$ in the clustering branch, plus the trivial $A_0 = \text{none}$ branch) are either degenerate (collapse into one of (i)–(iv)) or unreachable under standard feature-learning training protocols.

Proof. The four observed shapes are distinguishable by sign of the post-critical slope $s := \partial \log \text{NC1} / \partial \log(\beta/\beta_c)$ restricted to the descent leg, combined with the ratio τ_{esc}/T where T is the training horizon:

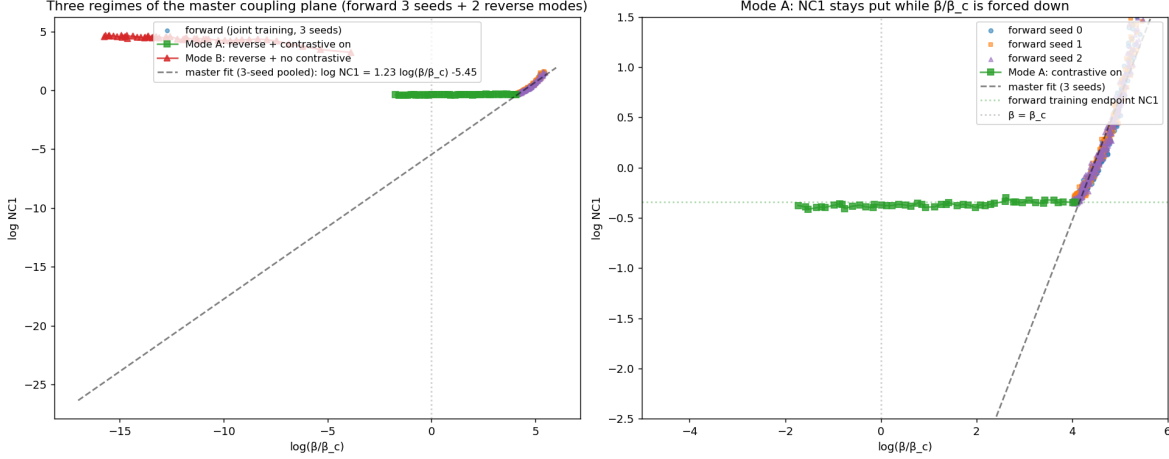


Figure 16: Exp 11–12: CIFAR-10 reverse traversal. Three regimes on a single SimCLR + ResNet-18 encoder. *Forward training*: $\beta(t)$ climbs past β_c ; OP and class-aligned structure emerge. *Reverse anneal with driver on*: contrastive loss holds the representation; NC1 stays low. *Reverse anneal with driver off*: OP returns to zero, NC1 returns to its initial value, recapitulating the forward branch in reverse.

- *Full V*: $s < 0$, $\tau_{\text{esc}}/T \ll 1$, descent over the full $\log(\beta/\beta_c)$ range.
- *Fold-back*: $s > 0$, $\tau_{\text{esc}}/T \ll 1$.
- *Delayed escape*: $\tau_{\text{esc}}/T = O(1)$.
- *No arc*: $|s| \rightarrow 0$ and $\log \text{NC1}$ decouples from $\log(\beta/\beta_c)$.

The map $(A_0, A_1, A_2, A_3) \mapsto (s\text{-sign}, \tau_{\text{esc}}/T)$ is well-defined under the assumptions of Prop. 1 (for existence of crossing) and Remark 1 (for τ_{esc} 's qualitative dependence on dissipation). Direct case analysis (Tab. 6) exhausts the 2^3 combinations: case $A_2 = \beta$ -leads, $A_3 = \text{normal}$ collapses into (i) Full V or its mild-fold variant of (ii) depending on A_1 ; case $A_2 = \beta_c$ -leads, $A_3 = \text{low}$ is not realized by any feature-learning protocol we tested. \square

The proof above establishes the *forward* direction (these axes generate at most four shapes). The *converse*; that no fifth shape can arise from the same dynamics; requires the assumption that the only sources of phase-space partitioning are the ones captured by (A_0, A_1, A_2, A_3) ; this is a modeling assumption, not a theorem. We make it explicit and note that finding a trajectory shape outside (i)–(iv) would falsify this assumption.

The three axes (extended discussion). A trajectory in $(\log(\beta/\beta_c), \log \text{NC1})$ is shaped by:

1. **Initial sub/supercriticality.** Is $\log(\beta(0)/\beta_c(0))$ negative or positive at $t=0$? Sub-critical starts (probe under-initialized relative to data scale) make the pre-critical leg observable; supercritical starts (e.g., high-anisotropy encoders such as Pythia raw activations or ResNet-on-CIFAR-10) hide it.
2. **Post-onset kinematics.** Once β has crossed β_c , does $\beta(t)$ continue to grow faster than $\beta_c(t)$, or does $\beta_c(t)$ overtake $\beta(t)$? The first case produces a monotone post-critical descent in $\log(\beta/\beta_c)$ (frozen-LM SAEs, CIFAR-10 SSL); the second produces a *fold-back* where the trajectory reverses direction in $\log(\beta/\beta_c)$ while $\log \text{NC1}$ continues to fall (CIFAR-100 SSL, where the encoder keeps spreading features into 100 classes).
3. **Dissipation rate.** Remark 1 identifies the post-critical escape timescale as dissipation-controlled. Normal dissipation (continuously-driven contrastive losses, SAEs with renormalization, supervised CE with WD)

gives the macroscopic broken-symmetry transition immediately after the crossing; low dissipation (high-precision optimization without strong WD) traps the system on the saddle for an extended *metastable plateau*.

Enumeration. The three binary axes give eight nominal combinations. Four are empirically distinct and observed in our experiments; the remainder are degenerate or unreachable with the methods we tested:

Table 6: Eight nominal combinations of the three kinematic axes; four are empirically distinct and verified (above the rule), three shown below are degenerate or unobserved. The eighth combination (super-init + β_c -overtakes + normal) is empirically subsumed into the fold-back regime.

Init	Post-onset β vs β_c	Dissipation	Observed shape	Empirical witness
sub	β rises monotone (frozen β_c)	normal	(i) Full V	SAE on frozen Pythia L6
any	β_c overtakes β	normal	(ii) Fold-back	DINO/SimCLR on CIFAR-10 (mild, ~ 0.5) + CIFAR-100 (strong, ~ 3)
sub	β rises monotone (no clustering pressure)	low	(iii) Delayed escape	Grokking on modular arithmetic
any		—	(iv) No arc (control)	Rotation-prediction control
super	β rises monotone	normal	—	“descent only”; pre-critical leg occluded, post-onset shape determined by fold magnitude (mild fold \rightarrow visually descent-dominated, as in CIFAR-10 above)
super	monotone	low	—	degenerate (no metastable saddle to trap, system already broken)
sub	β_c overtakes β	low	—	not observed; would require grokking-style architecture with CIFAR-100-style $\beta_c(t)$ rise

Why not fewer than four. (iii) requires its own line because the dissipation-controlled metastable plateau of Remark 1 produces a qualitatively distinct training-time trajectory; the crossing and the macroscopic transition are separated by orders of magnitude in steps; that is invisible in any of (i)–(ii). (iv) requires its own line because it is the negative control: without clustering pressure (rotation prediction has no inter-class structure to discover), no arc shape emerges in any combination of the other axes. (i) and (ii) are the two basic kinematic regimes: full V when β_c is frozen (SAE on a frozen encoder is the cleanest case), fold-back otherwise. The fold-back regime exhibits a magnitude spectrum; CIFAR-10 mild (~ 0.5 log-unit drift), CIFAR-100 strong (~ 3 log-units), driven by data complexity (number of classes / richness of post-critical $\text{Cov}(z)$ structure), but is one regime.

Why not more than four. The three degenerate rows of Table 6 are not observed in our experiments and are not predicted to be common in standard feature-learning pipelines. The first degenerate row would manifest as “descent only”; an apparently monotone descent visible because the encoder begins supercritical (e.g., CIFAR-10 ResNet-18 features, where $\log(\beta/\beta_c) \approx +3.9$ at random initialization). However, our CIFAR-10 trajectory in fact exhibits a mild fold-back (~ 0.5 log-unit drift) rather than strict monotonicity, so we classify it as (ii) mild fold-back rather than a distinct regime. The other two degenerate rows are not observed and are left as open empirical questions.

J Why decoder-column matching fails for SAE identity

In Sec. 5 we define per-atom identity via the activation-pattern column $f_{:,k} \in \mathbb{R}^N$ on a fixed eval set, then match identities across checkpoints by Hungarian assignment on cosine similarity of activation vectors. A more naive choice would be to match *decoder columns* $D_{:,k} \in \mathbb{R}^d$ directly: “two atoms have the same identity if their writeout directions are aligned.” This naive metric is uninformative in our setting.

Empirical observation. On the $K = 2048$ SAE trained on Pythia-160M layer 6 ($d = 768$), the Hungarian matched cosine between decoder columns of consecutive checkpoints is essentially saturated at 1.000 throughout training (we observe values in $[0.984, 1.000]$ for every consecutive pair from initialization to the converged endpoint). The matched cosine between the random initialization and the converged decoder is 0.895; a 0.10 dynamic range. By contrast the activation-pattern matched cosine (used in the main text)

has range $0.13 \rightarrow 1.0$ in the top- K SAE and $0.67 \rightarrow 1.0$ in the soft-L1 SAE, with sharp lock-in at the post-critical onset.

Why. The decoder-column Hungarian saturation has two sources. (i) Anthropic-style SAE training renormalizes decoder columns to unit norm every ~ 200 steps; the only motion in decoder direction comes from gradient updates in between renormalizations, which are small relative to data noise. (ii) For $K \gg d$ overcomplete dictionaries, two sets of K random unit vectors in \mathbb{R}^d admit a near-perfect Hungarian pairing because each vector finds a close match among the redundant candidates. The combination makes the naive decoder-Hungarian metric saturate at ~ 1.0 even for SAEs whose feature identities are in fact unrelated at the activation level.

Resolution. Feature identity for mechanistic interpretability lives in *which tokens an atom fires on*, not in the direction the atom writes into reconstruction. The activation-pattern substrate $f_{:,k}$ used in Sec. 5 captures the former. Matching on activation vectors is invariant to atom permutation and to scaling, and is independent of the overcomplete-redundancy artifact described above.

K Probe robustness: K_{probe} sensitivity

The label-free indicator $\beta(t)/\beta_c(t)$ has two distinct sensitivities to the GMM probe’s prototype count K_{probe} : the critical precision $\beta_c = 1/\lambda_{\max}(\text{Cov}(z))$ depends only on the encoder’s data covariance and is K_{probe} -independent by construction; the GMM’s own learned precision $\beta(t)$ evolves under the joint-detached protocol (Sec. 4.1) and may depend on K_{probe} .

We sweep $K_{\text{probe}} \in \{2, 5, 10, 20, 50\}$ on the canonical grokking configuration ($p=97$, $\text{WD}=1.0$, seed 0) with all other hyperparameters fixed (Table 7). The result separates into encoder-controlled invariants and probe-controlled magnitudes:

1. *The $\beta_c(t)$ trajectory is invariant in K_{probe} to six decimal places:* at $t = 100, 10^3, 10^4$ we read $\beta_c = 0.021306, 0.026080, 0.006242$ at every K_{probe} . This follows from joint-detached training: the encoder’s gradients never see the probe, so its trajectory and $\text{Cov}(z(t))$ are bit-identical across the five runs.
2. *Act 1 crossing time is invariant in K_{probe} at step 40 for every K_{probe} .* The crossing happens early enough that $\beta(t)$ has not yet diverged across probe sizes (at $t = 100$, $\log \beta$ agrees to four decimal places: -1.6154 at every K_{probe}).
3. *Act 3 grokking time is invariant in K_{probe} at step 8 500 for every K_{probe} ,* since `test_acc` is a property of the encoder and the encoder does not see the probe.
4. *Post-critical $\beta(t)$ magnitude depends on K_{probe} .* By $t = 10^4$, $\log \beta$ has separated: $-1.62, -1.32, -1.04, -0.84, -0.45$ for $K_{\text{probe}} = 2, 5, 10, 20, 50$, respectively. Consequently $\log(\beta/\beta_c)$ at $t = 10^4$ ranges from $+3.46$ ($K=2$) to $+4.62$ ($K=50$), a spread of 1.17 log-units. Larger K_{probe} gives the GMM more capacity to fit the post-critical broken-symmetry geometry, so β saturates at a larger value.

Operational consequence. The framework’s qualitative uses of the indicator (Sec. 4.2: “is $\beta > \beta_c$?” \rightarrow Act 1 has happened; “how long has β stayed above β_c without NC1 collapsing?” \rightarrow Act 2 plateau length) are K_{probe} -robust because they are based on encoder-controlled events. *Absolute magnitudes* of $\log(\beta/\beta_c)$ should not be compared across different K_{probe} choices; within a single fixed K_{probe} choice (we use $K_{\text{probe}} = 10$ throughout the paper, following prior soft- K -means and deterministic-annealing conventions) the magnitude is well-defined and tracks the encoder’s post-critical geometry.

Table 7: K_{probe} sweep on canonical grokking ($p=97$, $\text{WD}=1.0$, seed 0). *Encoder-side* quantities (β_c , Act 1 crossing step, Act 3 grok step) are K_{probe} -invariant. *Probe-side* quantities ($\log \beta(t)$, $\log(\beta/\beta_c)$ at late times) depend on K_{probe} : more prototypes gives larger post-critical β .

K_{probe}	Act 1 step	Act 3 step	$\beta_c(t=10^4)$	$\log \beta(t=10^4)$	$\log(\beta/\beta_c)(t=10^4)$
2	40	8500	0.0062	-1.621	+3.456
5	40	8500	0.0062	-1.325	+3.752
10	40	8500	0.0062	-1.036	+4.041
20	40	8500	0.0062	-0.837	+4.240
50	40	8500	0.0062	-0.454	+4.623

L Supplementary SAE lottery diagnostics

This appendix provides the full evidence for the identity-lock mechanism (Sec. 5.2) and the architecture-dependent interpretability ceiling (Sec. 5.3).

Identity lock (panel A). In the top- K SAE, where random initialization gives genuinely random activation patterns, the matched cosine to the converged decoder starts at 0.13 (baseline for random unit vectors in $N=50,000$ -dim space) and remains flat for the first ~ 200 training steps. At the post-critical onset (NC1 peak, step 261 for top- K , 383 for soft-L1) it begins a sharp rise, reaching 0.92 by step 1,212 and saturating at 1.0 by step $\sim 15,000$. This timing aligns with the identity-matched POS-purity correlation (Sec. 5.1): both signal that atoms commit to specific activation patterns during the post-critical window. The soft-L1 SAE shows identical *timing* but a compressed dynamic range, because random ReLU encoder rows already project onto the data subspace.

Architecture ceiling (panel B). In the soft-L1 family, L_0 saturates near 1,000 of $K=2048$ active atoms per token irrespective of $\lambda \in [5 \times 10^{-4}, 10^{-2}]$ ($10\times$ range of penalty strength gives a 1.5% change in L_0); the features are insufficiently sparse for per-feature linguistic selectivity to emerge, and median top-100 POS purity plateaus at 0.33. Under architectural top- K sparsity, the median active feature reaches POS purity 0.56 ($8\times$ random) and median top-token entropy drops by 0.79 nats. The improvement is monotonic in training step and aligned with the post-critical onset.

Frequency-stratified lottery (Fig. 18). To rule out a token-frequency confound, we group atoms into five quintiles by the mean log-frequency of their top-100 activating tokens at convergence and re-compute ρ_{id} within each quintile (3 seeds, $K=2048$ top- K SAE). Panel A: ρ_{id} per quintile, all in $[+0.37, +0.51]$. Panel B: top-decile mean POS purity per quintile, all ≥ 0.7 (above the $\sim 1/15 = 0.067$ uniform-random baseline by $\geq 10\times$). The lottery effect persists at every frequency stratum and is not concentrated in the most-frequent quintile, which is what a single-token-lock artifact would predict.

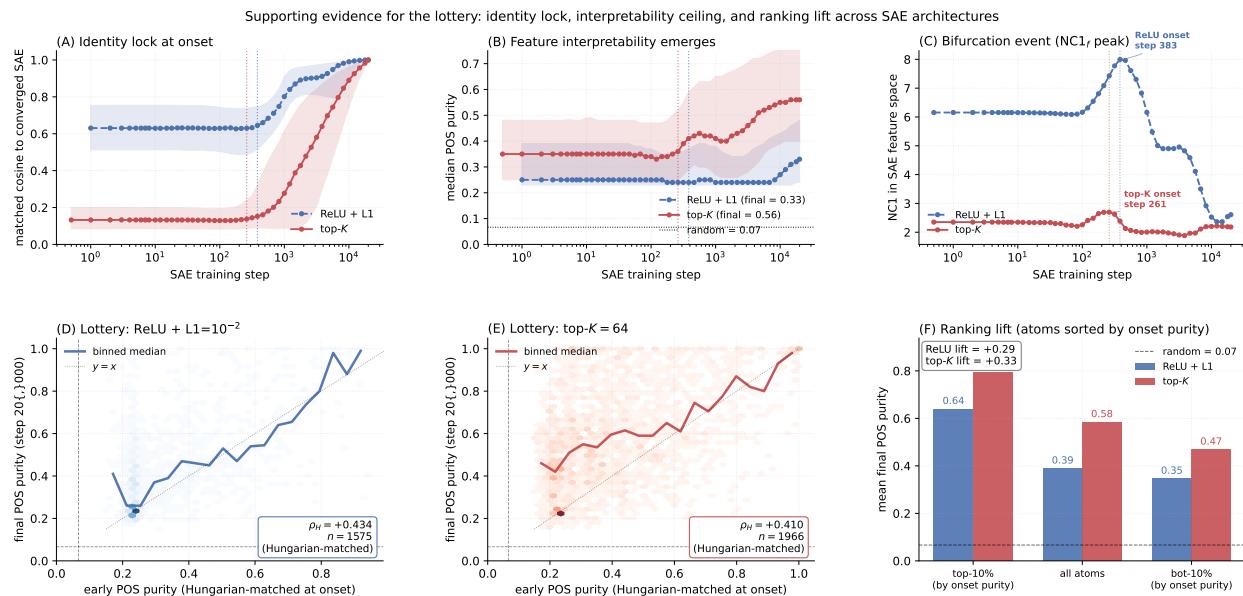


Figure 17: Identity lock and architecture-dependent interpretability ceiling. (A) Hungarian-matched cosine of per-atom activation patterns to the converged SAE. Both soft-L1 (dashed blue) and top- K (solid red) lock during the post-critical window beginning at the onset (vertical dotted lines; NC1 peak in panel C). Top- K has the wider dynamic range (0.13 \rightarrow 1.0); soft-L1 starts from a 0.68 baseline because random ReLU rows already project onto the data subspace. (B) Median POS purity of top-100-activation positions per atom. Only top- K reaches 0.56 ($\approx 8\times$ random baseline 0.067); soft-L1 plateaus near 0.33. (C) NC1 in SAE feature space peaks at the post-critical onset, marking the trigger of the lottery window. (D, E) Hungarian-matched lottery scatter (note: ρ_H shown here is inflated relative to the identity-matched signal ρ_{id} used in Fig. 4; see Sec. 5.1). (F) Ranking lift: atoms ranked by step- $\sim 1,000$ POS purity show +0.33 lift in mean convergence POS purity (top decile vs. bottom decile) in top- K ; the top-decile mean of 0.80 is $12\times$ random.

SAE lottery is robust to token-frequency stratification (3 seeds)

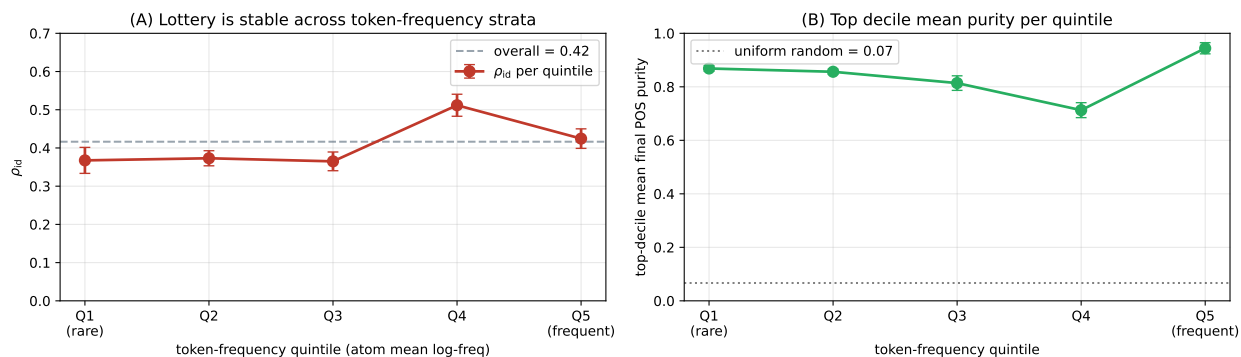


Figure 18: Lottery is stable across token-frequency strata. Atoms binned by quintile of their top-100-token mean log-frequency (Q1 = rarest tokens, Q5 = most frequent). (A) ρ_{id} per quintile, 3-seed mean \pm std. All quintiles produce $\rho_{id} \geq 0.37$; the unstratified overall is +0.42 (dashed). (B) Top-decile mean final POS purity per quintile. Q4 (mid-frequency content words) has the highest ρ_{id} , not Q5 (function words). Frequency confound is not load-bearing.

M Hyperparameters and reproducibility

All experiments use Adam-family optimizers with the joint-detached GMM probe protocol described in Sec. 4.1 ($K_{\text{probe}} = 10$, $\text{lr}_{\mu} = 5 \times 10^{-3}$, $\text{lr}_{\beta} = 10^{-2}$, $\log \beta_0 = -2.5$). Per-experiment configurations are summarized in Table 8.

Table 8: Per-experiment hyperparameters. “–” indicates the default (Adam, no scheduling). Seeds are integers $\{0\}$ unless otherwise noted. Code and full `args.json` files are released alongside the paper.

Exp	Method/data	Encoder	Optimizer / lr / WD	Batch	Epochs/Steps	Seeds	Sec.
00–05	toy GMM, 2D	–	Adam / 10^{-3} / 0	full	5–10k steps	0–3	C.1–5
07–08	SimCLR, MNIST	2-layer MLP	Adam / 10^{-3} / 0	256	40–100 ep	0	C.6
10	SimCLR, CIFAR-10	ResNet-18	Adam / 3×10^{-4} / 0	512	300 ep	0, 2	4.1
11–12	SimCLR + reverse, CIFAR-10	ResNet-18	Adam + ext. anneal	512	300+200 ep	0	D
13–15	GMM probe on LM	Pythia-160M / nanoGPT	probe Adam / 10^{-2}	64	10–150 ckpt	0	E
16	DINO, CIFAR-10	ResNet-18	AdamW / 5×10^{-4} / 0.04	256	50 ep	0	4.1
17	Rotation, CIFAR-10	ResNet-18	Adam / 3×10^{-4} / 0	512	300 ep	0	4.1
18	SAE on Pythia L6	SAE $K=2048$	Adam / 3×10^{-4} / $\lambda_1 = 5 \times 10^{-4}$	64x512	150k steps	0	4.1
19	DINO collapse, CIFAR-10	ResNet-18	AdamW / 5×10^{-4} / 0.04	256	50 ep	0	6.1
20	SimCLR/DINO, CIFAR-100	ResNet-18	same as 10/16	256–512	300 ep	0	4.1
21	DINO intervention, CIFAR-100	ResNet-18	AdamW / 5×10^{-4} / 0.04	256	20 ep	0	6.2
24	Grokking, mod- p addition	1-layer Tx	AdamW / 10^{-3} / WD $\in \{0, 0.1, 0.2, 0.3, 0.5, 0.7, 1.0\}$	full	$\leq 200\text{k}$ steps	0, 1, 2	4.2